





Dy adsorption on and intercalation under graphene on 6H-SiC(0001) surface from first-principles calculations

Yong Han ^{*}, James W. Evans , and Michael C. Tringides 
 Ames Laboratory, U.S. Department of Energy, Ames, Iowa 50011, USA
 and Department of Physics and Astronomy, Iowa State University, Ames, Iowa 50011, USA

 (Received 5 May 2021; revised 26 June 2021; accepted 1 July 2021; published 21 July 2021)

Previous experimental observations motivate clarification of configuration stabilities and kinetic processes for intercalation of guest atoms into a layered van der Waals material such as a graphene-SiC system. From our first-principles density functional theory (DFT) calculations, we analyze Dy adsorption and intercalation for graphene on a 6H-SiC(0001) surface, where the system includes two single-atom-thick graphene layers: the top-layer graphene (TLG) and the underling buffer-layer graphene (BLG) above the terminal Si layer. Our chemical potential analysis shows that intercalation of a single Dy atom into the gallery between TLG and BLG is more favorable than adsorption on TLG but that intercalation into the gallery underneath BLG is highly unfavorable. We obtain diffusion barriers of ~ 0.45 and 0.54 eV for a Dy atom diffusing on and under TLG, respectively. We find that the direct penetration of a Dy atom from the graphene top into the gallery under TLG is almost inhibited below a temperature of ~ 1400 K due to a large global barrier of at least ~ 3.5 eV. Instead, we find that a single Dy atom on TLG can easily intercalate by crossing a TLG step (e.g., a zigzag step presaturated by a Dy chain or a reconstructed zigzag step zz57). We also perform DFT calculations for different Dy coverages to demonstrate how the favorability of Dy intercalation, as well as the corresponding interlayer spacings, depend on the coverage. Consequently, we can provide general insight and guidance for extensively studied systems involving intercalation of foreign atoms into graphene on a SiC substrate.

DOI: [10.1103/PhysRevMaterials.5.074004](https://doi.org/10.1103/PhysRevMaterials.5.074004)

I. INTRODUCTION

Intercalation into few-layer van der Waals (vdW) materials [commonly called two-dimensional (2D) materials] by foreign guest atoms is rapidly becoming an attractive research area due to the strong need to develop next-generation energy-storage technologies and optoelectronic devices [1–3]. Among many types of 2D vdW materials, intercalation into epitaxial graphene on a SiC substrate has been heavily reported [4]. The initial motivation for such studies is that the intercalation of specific foreign species into the interface (or gallery) between the buffer-layer graphene (BLG) and SiC substrate can physically and electronically decouple the BLG from the SiC substrate to consequently obtain a quasifreestanding graphene layer [5–9]. Even more interestingly, such studies also result in important findings, e.g., superconductivity by Ca [10–14] and Li [15] intercalation; performance-enhanced graphene transistors [16] and quantum Hall effects [17] by H intercalation; manipulating Dirac cones in the band structure by Cu [18], Yb, and Dy [19] intercalation; a metal-dielectric transition by Sn intercalation [20]; tuning doping levels of graphene by Yb [21], Sn, and Ge [22] intercalation; a semiconductor-to-metal transition by Au intercalation [23], etc.

Undoubtedly, these various findings suggest promising applications. However, realization of such a goal depends on

the thermodynamic stability of the intercalated phase since it determines the temperature range where the grown heterostructure is operational. Therefore, theoretical analysis for stabilities of configurations associated with intercalation as well as understanding the kinetics of the intercalation process are fundamentally important. However, such analyses currently reported in literature are rare and therefore far from sufficient to provide insight into detailed behavior for many systems of interest.

Existing experimental observations still need further clarification of configuration stabilities for intercalation, especially for complex systems like guest atoms intercalated under graphene on a SiC substrate. An example is the case of Ca intercalation into few-layer graphene on a SiC substrate to form the thinnest limit of superconducting film, where several recent studies gave seemingly conflicting results. The intercalated Ca layer was observed to be in the gallery under the top-layer graphene (TLG) from the low-energy electron diffraction (LEED) experiments of Kanetani *et al.* [11] and the reflection high-energy electron diffraction experiments of Ichinokura *et al.* [14]. However, the same group also found that the intercalated Ca layer is in the gallery between the top-bilayer graphene and BLG when they used the rocking curve analysis for positron scattering [24]. Zhang *et al.* [25] found that the intercalated Ca layer was always in the top gallery from scanning tunneling microscopy (STM) experiments and density functional theory (DFT) calculations. A fifth study from Kotsakidis *et al.* [26] using LEED, STM, and DFT found that the Ca layer must be under the BLG. Clearly, this situation

^{*}y27h@ameslab.gov

needs further investigation and requires an appropriate way to compare intercalation under the same conditions, e.g., from DFT calculations.

For multiple metal guest elements, it was recently demonstrated that it is difficult or impossible to directly penetrate the perfect TLG of graphite into the gallery beneath the TLG in the typical experimental temperature range <1500 K. This feature likely reflects a large energy barrier for the penetration. Thus, to effectively realize metal intercalation under the surface of graphite, a preprepared ion-bombarded graphite surface is always needed, where the guest metal atoms (e.g., Dy, Cu, Ru, Fe, and Pt) can intercalate through the portal defects [27–35]. However, previous experiments (including our own experiments for rare-earth metals Dy, Eu, and Gd [36,37]) show that many types of guest elements can intercalate into epitaxial graphene on a SiC substrate [4] without a preprepared ion-bombarded top surface. Thus, it is desirable to analyze and understand the kinetic process for a given guest atom intercalating this system.

In this paper, we perform first-principles DFT calculations for Dy as the prototype guest atoms to intercalate graphene on a $6H$ -SiC(0001) substrate with the C-Si-C-Si-...-C-Si stacking sequence from bottom toward top (where “ $6H$ ” denotes the ABCACB stacking along the [0001] direction of a hexagonal structure and is sometimes omitted below). To avoid any confusion, it is necessary to clarify the notation used in this paper. Our graphene-SiC system in this paper includes two single-atom-thick graphene layers above the terminal Si layer: the TLG and the underlying BLG. We denote the gallery between BLG and the terminal Si layer as the “BS gallery” and denote the gallery between BLG and TLG as the “BT gallery.” In literature, the BLG is commonly called the zero-layer graphene (ZLG), and the TLG is commonly called the single-layer graphene (SLG). In this paper, we use TLG and BLG instead of ZLG and SLG, respectively.

By calculating the chemical potentials of Dy at different positions, we will analyze the thermodynamic favorability of various configurations. To analyze the kinetic process, we will calculate the binding energy landscapes and diffusion barriers for a single Dy atom transferred from the top terrace to different types of TLG steps and then to the gallery underneath the TLG. We also analyze the coverage dependences of the chemical potential of Dy and the corresponding interlayer spacings. Such analysis will facilitate interpretation of experiments, where Dy intercalation for this system has been confirmed [37]. Our more recent Dy intercalation studies using high-resolution LEED and STM have focused on the question of developing robust experimental methods of determining unambiguously the Dy metal location as a function of deposited Dy and annealing temperature. The present theoretical work of investigating the intercalation preference for the location of Dy as a function of intercalated Dy amount is relevant to this major question. The studies in this paper for Dy intercalation are also instructive for understanding the differences found experimentally for Ca intercalation under bilayer graphene (as described above) and for identifying the superconductivity mechanism in Ca since the electronic properties and band structure of the intercalated metal layer strongly depend on the location and structure of the intercalated metal layer.

This paper is organized as follows. Section II describes our DFT method used in this paper. In Sec. III, we discuss and compare different models for a clean graphene-SiC system without guest Dy atoms. In Secs. IV and V, we show our DFT results for a single Dy atom plus the graphene-SiC system without and with TLG steps, respectively. In Sec. VI, we discuss the binding energy landscapes and intercalation of a single Dy atom via TLG steps. In Sec. VII, we show the DFT results for higher Dy coverages and provide the information for the coverage dependences of the chemical potentials of Dy and the corresponding interlayer spacings. In Sec. VIII, we make a summary. Additional information is provided in Appendixes A–D.

II. DFT METHODOLOGY

For all first-principles DFT calculations in this paper, we use the Vienna *Ab initio* Simulation Package (VASP) code [38] with the projector-augmented-wave pseudopotentials [39] developed by the VASP group. The optB88-vdW functional [40] is used for electron-electron exchange correlations. This functional includes the vdW interactions, and its application for various vdW materials with metals [28–35,41–43] has already been proven very successful. A benchmark analysis for bulk properties of $6H$ -SiC and hexagonal close-packed (hcp) Dy is provided in Appendix A with the reasonable results. The properties of graphite and graphene predicted using the same DFT method as in this paper have closely matched experimental data [31,41].

In this paper, we focus on the systems involving TLG or BLG supported by a Si-terminated $6H$ -SiC(0001) substrate. To avoid any confusion, here, we emphasize that the TLG or the BLG is graphene with one C single-atom-thick layer. During energy minimization, all atoms are relaxed except that some atoms (or coordinates of some atoms) are fixed, as specified for different surface systems in the following sections. For the bottommost C single-atom-thick layer of SiC, the dangling bonds of all C atoms are always passivated by pseudo-H atoms. The surface system is modeled as a periodic slab with the vacuum thickness ≤ 1.8 nm between two adjacent slabs, and the k mesh is chosen based upon the supercell size. If the force exerted on each relaxed atom is <0.01 eV/Å, the total energy convergence is reached. The energy cutoff is set to be 550 eV. Spin polarization and dipole corrections are considered for all surface systems. To obtain the energy barriers of various diffusion processes of a Dy atom, we use the climbing image nudged elastic band (CINEB) method [44] to calculate the minimum energy paths (MEPs).

III. CLEAN GRAPHENE ON SiC WITHOUT GUEST DY ATOMS

Before analyzing adsorption or intercalation of Dy, we first analyze clean graphene on SiC without any guest Dy atoms. Because of the lattice mismatch between the graphene layer and the SiC(0001) substrate, the choice of supercell size for DFT calculations needs to be considered carefully. Previous experimental observations suggested that graphene layers grown on the SiC substrate display a $(6\sqrt{3} \times 6\sqrt{3})R30^\circ$ superlattice ordering [45,46] which evolves at lower tem-

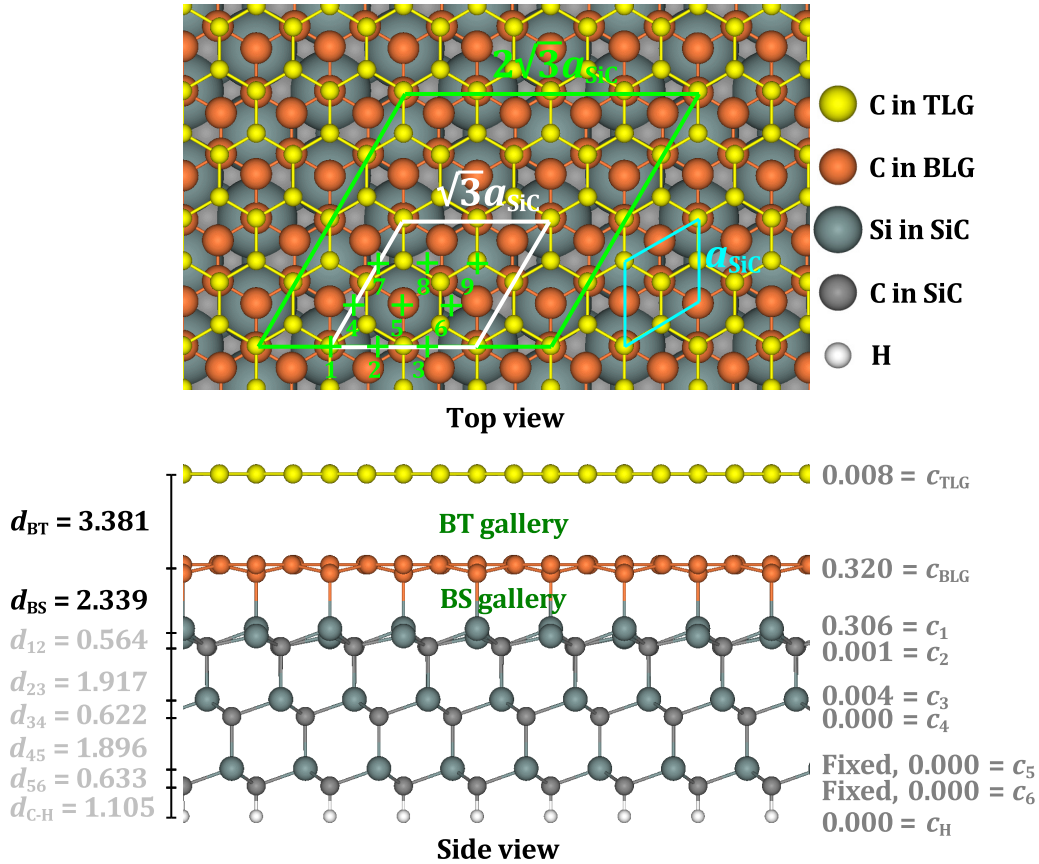


FIG. 1. Fully relaxed structure of two graphene layers [top-layer graphene (TLG) and buffer-layer graphene (BLG)] on Si-terminated 6H-SiC(0001) substrate from our density functional theory (DFT) calculation. The SiC substrate has a thickness of six single-atom-thick layers with a C-Si-C-Si-C-Si stacking sequence from bottom to top. The bottommost C and Si single-atom-thick layers are fixed during relaxation, and the dangling bonds of C atoms are passivated by pseudo-H atoms. The green frame in the top view indicates a supercell ($4a_{\text{C}}^* \times 4a_{\text{C}}^*$ matching $2\sqrt{3}a_{\text{SiC}} \times 2\sqrt{3}a_{\text{SiC}}$) used in the DFT calculation. The white and cyan frames in the top view indicate a rotation of 30° from the $a_{\text{SiC}} \times a_{\text{SiC}}$ unit cell to the $\sqrt{3}a_{\text{SiC}} \times \sqrt{3}a_{\text{SiC}}$ unit cell. The BT gallery is between BLG and TLG, while the BS gallery is between BLG and the terminal Si layer. The left of the side view shows the interlayer spacings (d_{BT} , d_{BS} , d_{12} , d_{23} , d_{34} , d_{45} , d_{56} , and $d_{\text{C-H}}$), each of which is defined as the difference of average heights of atoms between two corresponding single-atom-thick layers. The right of the side view shows the corrugations (c_{TLG} , c_{BLG} , c_1 , c_2 , c_3 , c_4 , c_5 , c_6 , and c_{H}), each of which is defined as the height difference between the highest atom and the lowest atom within the corresponding single-atom-thick layer. All interlayer spacings and the corrugations are in units of angstroms.

peratures from superstructures including the $(\sqrt{3} \times \sqrt{3})R30^\circ$ superlattice ordering [45]. Corresponding to these two types of reconstruction, two unit-cell models can be constructed: $13a_{\text{C}}^* \times 13a_{\text{C}}^*$ matching $6\sqrt{3}a_{\text{SiC}} \times 6\sqrt{3}a_{\text{SiC}}$ (Model 1) and $2a_{\text{C}}^* \times 2a_{\text{C}}^*$ matching $\sqrt{3}a_{\text{SiC}} \times \sqrt{3}a_{\text{SiC}}$ (Model 2). If the lateral lattice constants of SiC(0001) and graphene take the optB88-vdW values $a_{\text{SiC}} = 3.09545 \text{ \AA}$ and $a_{\text{C}} = 2.464 \text{ \AA}$ (see Appendix A), Model 1 corresponds to a tiny laterally tensile strain $(a_{\text{C}}^*/a_{\text{C}} - 1) \times 100\% \approx 0.4\%$ with a strained overlayer graphene lattice constant $a_{\text{C}}^* = 6\sqrt{3}a_{\text{SiC}}/13 \approx 2.475 \text{ \AA}$, while Model 2 corresponds to a relatively larger lateral tensile strain $(a_{\text{C}}^*/a_{\text{C}} - 1) \times 100\% \approx 8.8\%$ with $a_{\text{C}}^* = \sqrt{3}a_{\text{SiC}}/2 \approx 2.681 \text{ \AA}$. In the following DFT calculations for Dy adsorption and intercalation, we choose Model 2. For each required calculation in the sections below, we will construct a rhombus or rhomboid supercell with the size of $2ma_{\text{C}}^* \times 2na_{\text{C}}^*$ matching $m\sqrt{3}a_{\text{SiC}} \times n\sqrt{3}a_{\text{SiC}}$, or a rectangular supercell with the size of $2ma_{\text{C}}^* \times n\sqrt{3}a_{\text{C}}^*$ matching $m\sqrt{3}a_{\text{SiC}} \times 1.5na_{\text{SiC}}$ (or

$n\sqrt{3}a_{\text{C}}^* \times 2ma_{\text{C}}^*$ matching $1.5na_{\text{SiC}} \times m\sqrt{3}a_{\text{SiC}}$), where m and n are positive integers.

In Fig. 1, we use Model 2 to construct a rhombus supercell with $m = n = 2$ for a graphene-SiC system with a SiC substrate of six single-atom-thick layers (i.e., 3 Si and 3 C single-atom-thick layers), where the k mesh is taken to be $6 \times 6 \times 1$. This system includes 147 atoms: 100 C atoms, 36 Si atoms, and 12 H atoms for saturating the dangling bonds of the 12 bottommost C atoms. After full relaxation, the interlayer spacings from this optB88-vdW calculation are almost the same as those from the PBE-TS calculation by Sforzini *et al.* [9], but the corrugations are significantly smaller than theirs, as listed in Table I. The interlayer spacings and the corrugations are defined in the caption of Fig. 1.

As a comparison, we also use Model 1 to construct a rhombus supercell for a graphene-SiC system with a SiC substrate of 4 C single-atom-thick layers. The k mesh is taken to be $1 \times 1 \times 1$. This system includes 1216 atoms: 892 C atoms,

TABLE I. Interlayer spacings and corrugations from DFT calculations for four coverages of Dy. For the coverage of 0 ML (i.e., clean graphene-SiC system without Dy), the data are from Model 1, Model 2, and previous PBE-TS calculation [9]. For the coverages of $\frac{1}{16}$, $\frac{1}{4}$, and 1 ML, the data are from Model 2. The coverage of $\frac{1}{16}$ ML approximates a single isolated Dy atom. T (T1 or T2), BT, and BS stand for Dy on TLG, in the BT gallery, and in the BS gallery, respectively, as in Figs. 4, 10, and 11. T1 and T2 correspond to Figs. 10(a) and 10(b). The bold values highlight the interlayer spacings of intercalated galleries.

Coverage	0 ML			$\frac{1}{16}$ ML			$\frac{1}{4}$ ML				1 ML		
	Model 1	Model 2	[9]	T	BT	BS	T1	T2	BT	BS	T	BT	BS
d_{BT}	3.472	3.381	3.40	3.367	4.156	3.400	3.313	3.366	4.280	3.399	3.311	7.665	3.370
d_{BS}	2.525	2.339	2.36	2.332	2.283	4.374	2.334	2.340	2.186	4.433	2.329	2.180	7.453
d_{12}	0.607	0.564	0.55	0.576	0.593	0.596	0.569	0.566	0.631	0.653	0.575	0.631	0.646
d_{23}	1.906	1.917	1.92	1.915	1.911	1.917	1.917	1.917	1.901	1.895	1.916	1.902	1.894
d_{34}	0.592	0.622	0.61	0.625	0.626	0.633	0.622	0.623	0.633	0.632	0.624	0.633	0.629
d_{45}		1.896	1.90	1.896	1.895	1.895	1.896	1.896	1.894	1.894	1.896	1.894	1.894
d_{56}		0.633	0.62	0.633	0.633	0.633	0.633	0.633	0.633	0.633	0.633	0.633	0.633
d_{C-H}	1.108	1.105		1.105	1.105	1.105	1.105	1.105	1.105	1.105	1.105	1.105	1.105
c_{TLG}	0.694	0.008	0.45	0.107	0.252	0.006	0.052	0.241	0.060	0.002	0.068	0.072	0.010
c_{BLG}	1.227	0.320	0.86	0.321	0.581	0.093	0.321	0.327	0.550	0.036	0.316	0.494	0.162
c_1	0.334	0.306	0.78	0.257	0.338	0.600	0.297	0.303	0.067	0.208	0.255	0.098	0.106
c_2	0.203	0.001	0.30	0.002	0.137	0.151	0.005	0.003	0.156	0.114	0.001	0.150	0.063
c_3	0.110	0.004	0.21	0.002	0.070	0.069	0.004	0.004	0.066	0.071	0.000	0.067	0.026
c_4	0.000	0.000	0.14	0.001	0.030	0.030	0.001	0.001	0.031	0.005	0.000	0.029	0.031
c_5		0.000	0.08	0.000	0.000	0.000	0.000	0.000	0.000	0.000	0.000	0.000	0.000
c_6		0.000	0.05	0.000	0.000	0.000	0.000	0.000	0.000	0.000	0.000	0.000	0.000
c_H	0.009	0.000		0.001	0.001	0.001	0.000	0.001	0.000	0.000	0.000	0.000	0.000

216 Si atoms, and 108 H atoms, as illustrated in Fig. 2. After full relaxation, the corrugations become more prominent, but the interlayer spacings do not significantly change (see Table I), in contrast to the results from Model 2. Although Model 2 has a significant lateral strain of $\sim 8.8\%$, we expect that it would not substantially affect our results in this paper (e.g., a previous DFT analysis for graphene layers on Cu(111) slab suggests that the adhesion energy is almost independent of the lateral strain in a normal range [41]). In fact, Model 2 has been already widely used in literature [9,47–50], instead of Model 1, for which the computational cost is extreme, especially for the graphene-SiC system with guest atoms adsorbed or intercalated. Finally, it is worthwhile to mention that, from our above DFT calculations, the slabs in Figs. 1 and 2 are magnetic with the magnetic moments of $1.885\mu_B$ and $20.479\mu_B$, respectively, where μ_B is the Bohr magneton.

IV. ADSORPTION, INTERCALATION, AND DIFFUSION OF A SINGLE Dy ATOM WITHOUT TLG STEPS

Knowledge of energetics for a single isolated atom at the surface of a layered material is fundamental to assess the thermodynamic preference of intercalation vs adsorption for the guest atom [28,29,32–35,42,43], as well as related kinetic processes [27,51]. Predicting the geometric structure after the guest atom intercalates into the layered material is also instructive, e.g., interlayer spacings and surface corrugations can be experimentally measured as basic structural parameters.

Because our DFT calculations involve periodic boundary conditions (PBCs), it is not possible to strictly analyze an isolated atom with a finite supercell. In this paper, we choose

the rhombus supercell with a size of $2\sqrt{3}a_{SiC} \times 2\sqrt{3}a_{SiC} = 4a_C^* \times 4a_C^*$, as indicated by the green frame in Fig. 1. The k mesh is again set to be $6 \times 6 \times 1$. Each supercell includes only one Dy atom. This is equivalent to a coverage of $\frac{1}{16}$ monolayer (ML), where 1 ML has the definition that any $a_C^* \times a_C^*$ unit cell for graphene is occupied by one Dy atom to form a Dy ML. We expect that a system with such a low coverage of $\frac{1}{16}$ ML can be a good approximation to a single isolated Dy atom.

To search the energy minima of the Dy atom on TLG or in a gallery, we relax $N = l^2$ configurations with the Dy atom initially lying on equidistant grid points of a 2D $l \times l$ grid covering the unit-cell area of $\sqrt{3}a_{SiC} \times \sqrt{3}a_{SiC} = 2a_C^* \times 2a_C^*$ (i.e., the white frame in Fig. 1) in the already fully relaxed graphene-SiC supercell (i.e., the green frame in Fig. 1). Then by comparing the total energies and examining the geometries of all configurations after full relaxation, the energy minima can be found. In principle, to reliably obtain all possible minima, a larger l is required. In this paper, we set $l = 3$, which is expected to be sufficiently large (as verified from the MEPs for Dy atom diffusion below), i.e., we relax $N = l^2 = 9$ configurations, as indicated by the nine green crosses in Fig. 1. We denote any of the nine configurations for the Dy atom on TLG, in the BT gallery, or in the BS gallery as a letter a, b, or c followed by a number $i = 1, 2, 3, \dots, 9$, respectively. The initial configuration bi or ci is set by only shifting the Dy atom of the initial configuration ai along the direction vertical to the surface (i.e., the height direction) into the BT or BS gallery, as indicated by the inset in Fig. 3.

In Fig. 3, we plot the chemical potentials μ (see Appendix B for the definition) of the 27 fully relaxed structures described above. In Fig. 4, we show three configurations a4, b9, and c1, each of which corresponds to the lowest of nine μ

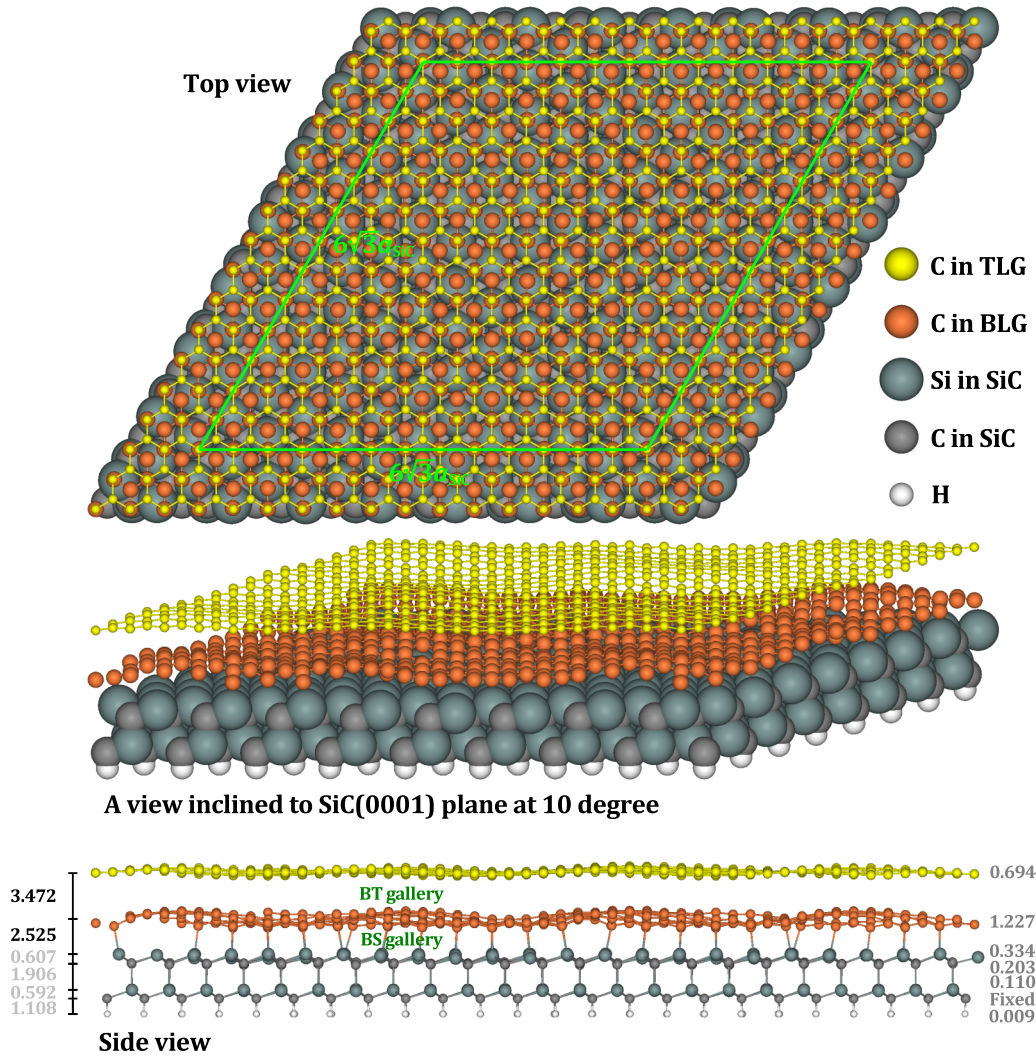


FIG. 2. Different views of fully relaxed structure of top-layer graphene (TLG) and buffer-layer graphene (BLG) on a Si-terminated SiC(0001) substrate with a thickness of four single-atom-thick layers from our density functional theory (DFT) calculation. The green frame in the top view indicates a supercell ($13a_c^* \times 13a_c^*$ matching $6\sqrt{3}a_{SiC} \times 6\sqrt{3}a_{SiC}$) used in the DFT calculation. The left of the side view shows the average interlayer spacings (in angstroms), and the right shows the corrugations (in angstroms) for each single-atom-thick layer. See the caption of Fig. 1 for other similar details.

values for the Dy atom on TLG, in the BT gallery, or in the BS gallery, respectively. The chemical potentials of a4, b9, and c1 are $\mu = -2.631, -4.606, \text{ and } +1.543$ eV. This indicates that the intercalation into the BT gallery is most favorable, while the intercalation into the BS gallery is highly unfavorable, i.e., the order for the thermodynamic favorability of an isolated Dy atom is $BT > \text{top} > BS$.

The interlayer spacings and corrugations of all layers are shown in Fig. 4 and listed in Table I as the Dy coverage of $\frac{1}{16}$ ML. By comparing with the clean graphene-SiC result in Fig. 1, the interlayer spacing for any BT or BS gallery without the Dy atom intercalated has only a tiny change, while the interlayer spacing for any BT or BS gallery with the Dy atom intercalated has a large increase: $\Delta d_{BT} = 4.156 - 3.381 = 0.775$ Å and $\Delta d_{BS} = 4.374 - 2.339 = 2.035$ Å. For the corrugations, there are variations for different layers. The corrugations ($c_{TLG} = 0.252$ Å and $c_{BLG} = 0.581$ Å) for the BT intercalation as well as the corrugation ($c_1 = 0.600$ Å) of

the top Si layer for the BS intercalation become significantly larger than those ($c_{TLG} = 0.008$ Å, $c_{BLG} = 0.320$ Å, and $c_1 = 0.306$ Å) for the clean graphene-SiC result. The increased interlayer spacings and corrugations are generally related to larger contributions to total energies from elastic strain effects when a guest atom is intercalated into the gallery [43].

To obtain the diffusion barriers of a Dy atom diffusing on TLG and in the BT gallery as well as the barrier for penetrating the TLG from top into BT gallery, we calculate three corresponding MEPs. For the diffusion on TLG, two CINEB endpoints are chosen to be the adjacent configurations a4 and a5 in Fig. 3. The MEP and trajectory between a4 and a5 from our DFT calculations is plotted in Fig. 5(a), and then the corresponding diffusion barrier $E_d^{\text{top}} = 0.446$ eV is obtained, as indicated by a vertical red arrow. For the diffusion in the BT gallery, we find the MEP and trajectory between b9 and b7 from our DFT calculations, as shown in Fig. 5(b). The corresponding diffusion barrier is obtained as $E_d^{\text{BT}} = 0.535$ eV, as

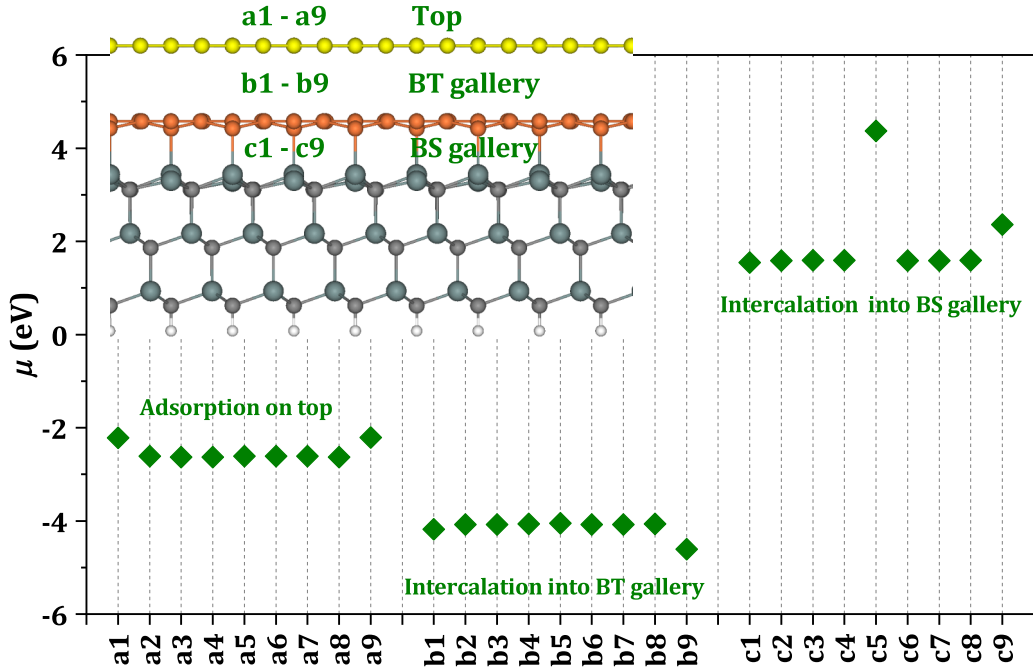


FIG. 3. Chemical potentials (μ) of fully relaxed structures for adsorption on top-layer graphene (TLG; configuration a1 to a9), intercalation into the gallery between buffer-layer graphene (BLG) and TLG (BT gallery; b1 to b9), or intercalation into the gallery between BLG and the terminal Si layer (BS gallery; c1 to c9). The initial positions of the Dy atom for these configurations are indicated in Fig. 1 by nine green crosses in a $\sqrt{3}a_{\text{SiC}} \times \sqrt{3}a_{\text{SiC}}$ unit cell. Initially, the position of the Dy atom has a shift from a1 to b1 or c1, from a2 to b2 or c2, ..., and from a9 to b9 or c9 (i.e., correspondingly from top to BT or BS gallery), as indicated in the inset.

indicated by a vertical red arrow. We also examined another MEP between b9 and b5 but with a higher barrier of ~ 0.8 eV, which then is not necessary to be specifically considered in our analysis below. For the penetration from the top into the BT gallery, we obtain a global energy barrier as $E_{\text{dp}} \gtrsim 3.5$ eV. The DFT calculations for the penetration process are very demanding, and the details as well as discussion will be separately published elsewhere [52].

V. ADSORPTION AND INTERCALATION OF A SINGLE Dy ATOM AT TLG STEPS

As analyzed above in Sec. IV, for a guest Dy atom on TLG of the graphene-SiC system, the global energy barrier $E_{\text{dp}} \gtrsim 3.5$ eV for directly penetrating TLG is large, so that intercalation into the BT gallery underneath TLG is difficult. For example, consider the penetration rate determined by the Ar-

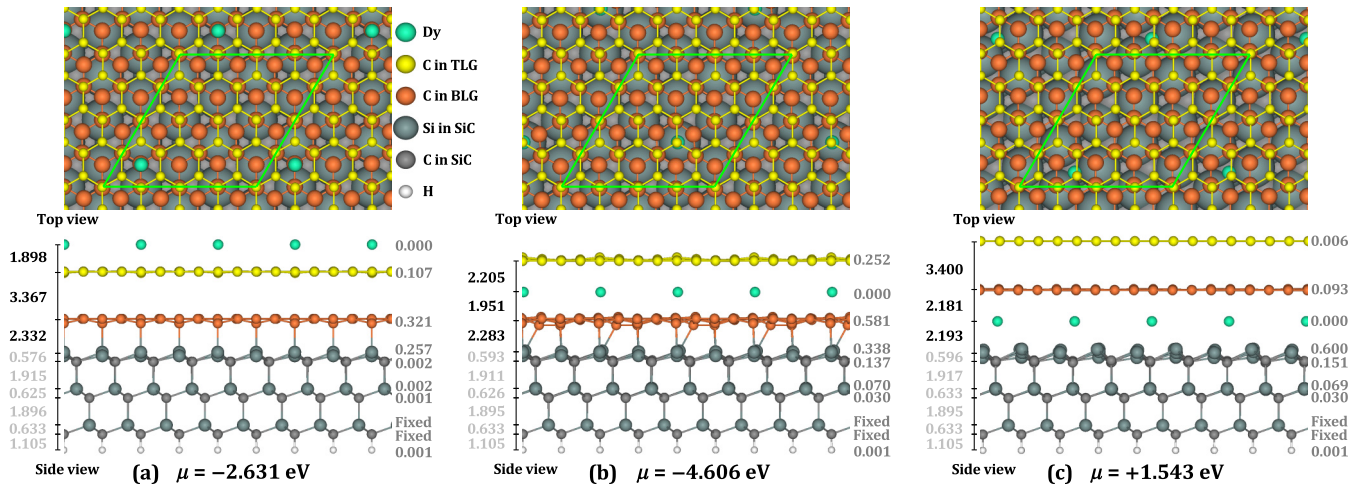


FIG. 4. Fully relaxed structures with the lowest μ values for a Dy atom (a) on top-layer graphene (TLG), (b) in the gallery between buffer-layer graphene (BLG) and TLG (BT gallery), and (c) in the gallery between BLG and the terminal Si layer (BS gallery) from our density functional theory (DFT) calculations, which correspond to a4, b9, and c1 in Fig. 3, respectively. The green frame in the top view indicates the $2\sqrt{3}a_{\text{SiC}} \times 2\sqrt{3}a_{\text{SiC}}$ supercell used in the DFT calculations. The left of the side view shows the interlayer spacings (in angstroms), and the right shows the corrugations (in angstroms) for each single-atom-thick layer.

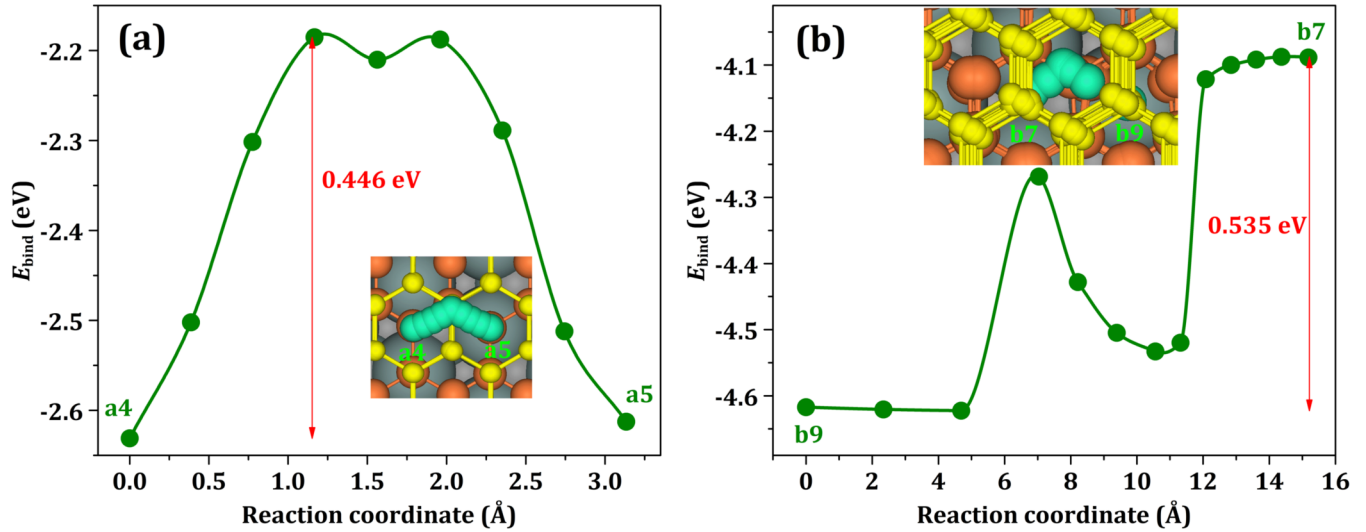


FIG. 5. Minimum energy paths (MEPs) (a) between endpoints a4 and a5 for a Dy atom on top-layer graphene (TLG), and (b) between endpoints b9 and b7 for a Dy atom in the gallery between buffer-layer graphene (BLG) and TLG (BT gallery), from our density functional theory (DFT) calculations with the climbing image nudged elastic band (CINEB) method, where a4, a5, b9, and b7 are the fully relaxed configurations in Fig. 3. The insets are the trajectories from one endpoint to another one. Green dots are the CINEB images, and the curves are from nonlinear interpolations. A trajectory is obtained by combining all evolving configurations corresponding to the CINEB images into one picture. The global diffusion barriers are indicated by the vertical red arrows.

rehius forms $r_{dp} = \nu e^{-\beta E_{dp}}$, where $\nu \approx 10^{13}/s$ is the attempt frequency, and $\beta = 1/(k_B T)$ is the inverse temperature with temperature T and Boltzmann constant k_B . Even for a high temperature $T = 1000$ K, the rate $r_{dp} = \nu e^{-\beta E_{dp}} \approx 10^{-5}/s$, which is very low for the penetration or intercalation.

Instead, a TLG step is expected to be able to act as a portal for intercalation. To confirm this expectation, in this section, we perform the DFT calculations for a single Dy atom plus a graphene-SiC system with stepped TLG (i.e., with incomplete TLG strips or ribbons and exposed BLG strips separated from the TLG strips by linear steps). Experimentally, multiple types of graphene step edge have been observed, including normal zigzag and armchair as well as various reconstructed edges, as discussed in our previous work for the Cu-graphite system [31]. Below, the calculations will involve three typical step edges for the TLG: zigzag, armchair, and $zz57$ (i.e., a reconstruction of zigzag step edge by a transition from a C_6 -ring sequence to a C_5 -ring-plus- C_7 -ring sequence [31]).

A. TLG zigzag steps

In the zigzag-step calculations, we use a rectangular supercell with the size of $2\sqrt{3}a_{SiC} \times 6a_{SiC}$ and the k mesh is taken to be $6 \times 3 \times 1$. For the structures of the TLG steps, we consider three configurations. The first configuration is $zz-1$, for which one zigzag C row is removed so that a narrow strip of exposed BLG is created with two zigzag steps within a supercell. The fully relaxed $zz-1$ is shown in Fig. 6(a). The configuration of $zz-1$ can be considered as an experimentally observed line between two intrinsic stacking domains in TLG [53–56]. The second configuration is $zz-3$, for which three zigzag rows are removed so that a wider strip of exposed BLG is created with two zigzag steps. The fully relaxed $zz-3$ is shown in Fig. 6(d). Because the strip of exposed BLG for $zz-3$

is sufficiently wide, the interactions between two steps can be neglected so that one of the steps can be approximated as an isolated zigzag step. Thus, $zz-1$ and $zz-3$ correspond to two limits: two steps separated by the narrowest strip of exposed BLG and one step approximately isolated, respectively. The third configuration is $zz-3-c$, for which a $zz-3$ step edge is predecorated by a Dy chain. The fully relaxed $zz-3-c$ is shown in Fig. 6(g). The consideration of $zz-3-c$ is motivated by our previous work for Cu-graphite systems [31].

For the $zz-1$ calculations, we initially position the Dy atom at two differently selected sites near the $zz-1$ step edge in Fig. 6(a) and then obtain two fully relaxed configurations in Figs. 6(b) and 6(c). From the symmetry and PBC of the system, two geometries in Figs. 6(b) and 6(c) are almost the same, but they have different magnetic moments (about $13.2\mu_B$ and $11.3\mu_B$, as listed in Table S2 in the Supplemental Material [57]), so their chemical potentials μ or binding energies E_{bind} (see Appendix B for the definition of E_{bind} as well as the relationship between μ and E_{bind}) have a relatively small difference of $\Delta\mu = \Delta E_{bind} = -9.336 - (-9.414) = 0.078$ eV.

For the $zz-3$ calculations, we initially position the Dy atom at two differently selected sites near the $zz-3$ step edge in Fig. 6(d) and then obtain two fully relaxed configurations in Figs. 6(e) and 6(f). From the symmetry of the system, two geometries in Figs. 6(e) and 6(f) are almost identical, but they have a relatively small chemical-potential or binding-energy difference of $\Delta\mu = \Delta E_{bind} = -7.804 - (-7.891) = 0.087$ eV due to different magnetic moments of about $14.3\mu_B$ and $10.3\mu_B$, as listed in Table S2 in the Supplemental Material [57].

For the $zz-3-c$ calculations, we also initially position the Dy atom at two different sites near the Dy chain in Fig. 6(g), but one is at a site on the side of the exposed BLG strip, and

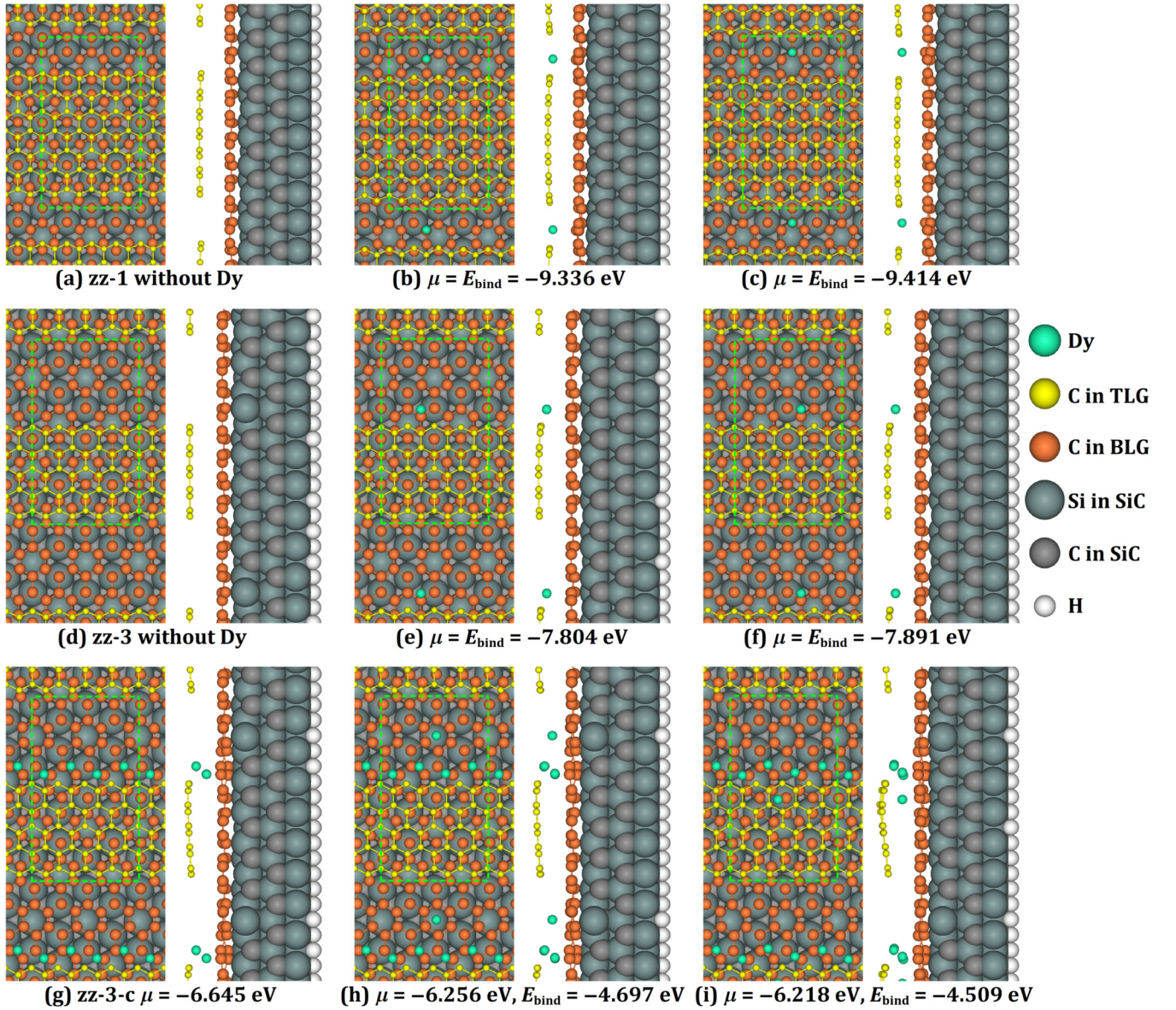


FIG. 6. Fully relaxed structures of three types of steps (zz-1, zz-3, and zz-3-c) with and without Dy atoms. The green dashed frame indicates the $2\sqrt{3}a_{\text{SiC}} \times 6a_{\text{SiC}}$ supercell used in our density functional theory (DFT) calculations. (a) Step zz-1 obtained by removing one zigzag row and then relaxing. (b) and (c) Two configurations by relaxing one Dy atom at two different initial sites near the zz-1 step and between two steps. (d) Step zz-3 obtained by removing three zigzag rows and then relaxing. (e) and (f) Two configurations by relaxing one Dy at two different initial sites near the zz-3 step and between two steps. (g) Step zz-3-c obtained by relaxing one Dy chain to saturate the zz-3 step. (h) and (i) Two configurations by relaxing one Dy atom at two different initial positions at the zz-3-c step: for (h), the Dy atom initially lies at a site near the saturated step and between two steps; for (i), the Dy atom initially lies at a site near the saturated step but beneath the top-layer graphene (TLG) ribbon. During energy minimization, except all relaxed atoms, the bottommost C and Si single-atom-thick layers are fixed. For (e), (f), (h), or (i), we also fix the lateral coordinates of four C atoms of the step edge without any Dy atom.

another one is at a site underneath the TLG ribbon. After full relaxations, we obtain the configurations in Figs. 6(h) and 6(i) with $E_{\text{bind}} = -4.697$ and -4.509 eV, respectively. Note that, in the zz-3-c case, the chemical potential μ of a Dy atom for a configuration is not equal to the corresponding E_{bind} because the total number of Dy atoms at the zz-3 step is >1 . The chemical potentials of three configurations in Figs. 6(g)–6(i) are $\mu = -6.645$, -6.256 , and -6.218 eV, respectively.

B. TLG armchair steps

In the armchair-step calculations, a rectangular supercell of $3a_{\text{SiC}} \times 4\sqrt{3}a_{\text{SiC}}$ with a k mesh of $6 \times 3 \times 1$ is chosen. For the TLG step structures, we consider only two configurations. The first configuration is ac-1, for which one armchair row is removed so that a narrow strip of exposed BLG is created with two armchair steps within the supercell. The fully relaxed ac-1 is shown in Fig. 7(a). Again, the configuration of ac-1 can be considered as a possible stacking domain boundary line, as

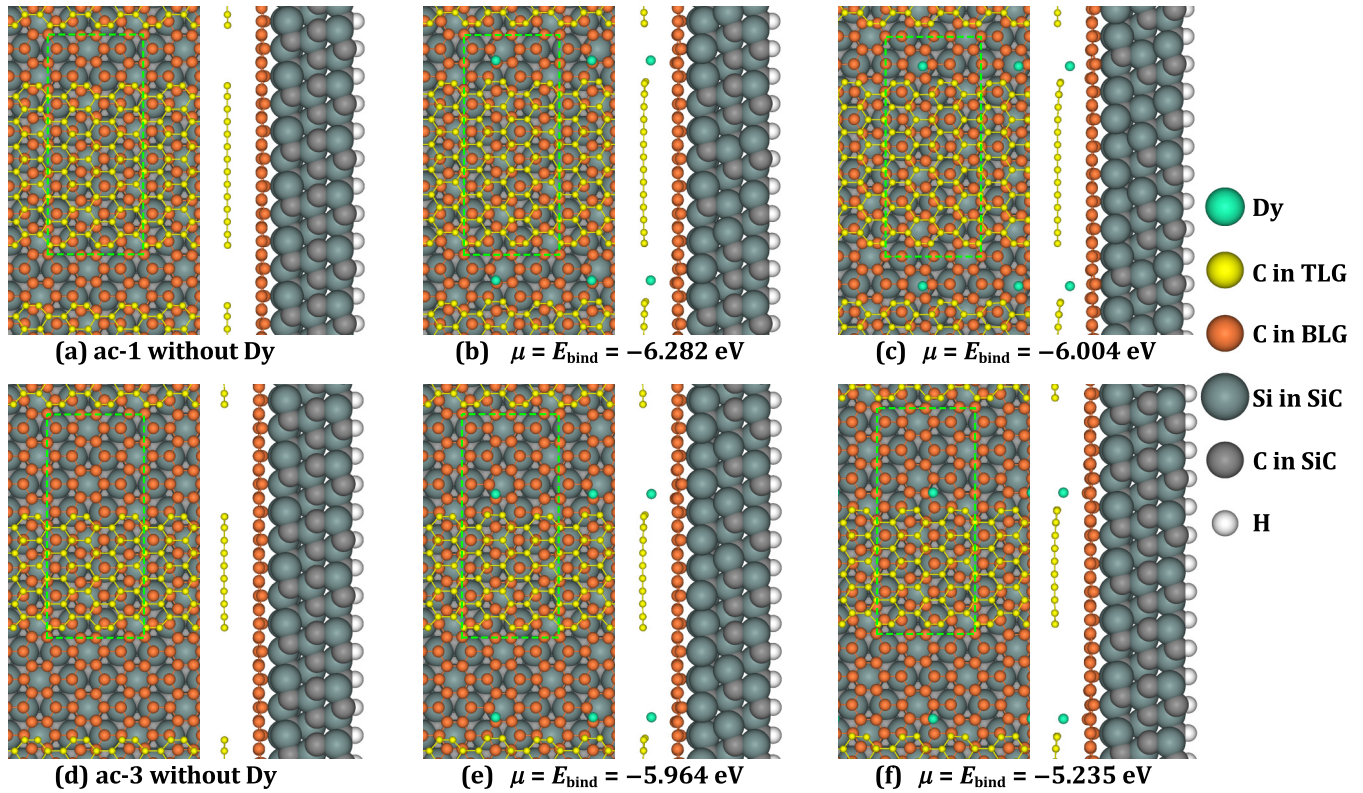


FIG. 7. Fully relaxed structures of ac-1 and ac-3 steps with and without Dy atoms. The green dashed frame indicates the $3a_{\text{SiC}} \times 4\sqrt{3}a_{\text{SiC}}$ supercell used in our density functional theory (DFT) calculations. (a) Step ac-1 is obtained by removing one armchair row and then relaxing. (b) and (c) Two configurations by relaxing one Dy atom at two different initial positions at the ac-1 step. (d) Step ac-3 is obtained by removing three armchair rows and then relaxing. (e) and (f) Two configurations by relaxing one Dy atom at two different initial positions at the ac-3 step. During energy minimization, except all relaxed atoms, the bottommost C and Si single-atom-thick layers are fixed. For (b), (c), (e), or (f), we also fix the lateral coordinates of four C atoms of the step edge without the Dy atom.

observed in experiments [53–56]. The second configuration is ac-3, for which three armchair rows are removed so that a wider strip of exposed BLG is created with two armchair steps. The fully relaxed ac-3 is shown in Fig. 7(d). Again, the strip of exposed BLG for ac-3 is sufficiently wide, and then the interactions between two steps can be neglected so that one of the steps can be approximated as an isolated armchair step.

For the ac-1 calculations, we initially select two different sites of the Dy atom near the ac-1 step edge in Fig. 7(a) and then obtain two fully relaxed configurations in Figs. 7(b) and 7(c). Two geometries in Figs. 7(b) and 7(c) are different. The configuration in Fig. 7(c) has a higher chemical potential or binding energy $\mu = E_{\text{bind}} = -6.004 \text{ eV}$ than $\mu = E_{\text{bind}} = -6.282 \text{ eV}$ for that in Fig. 7(b).

For the ac-3 calculations, we initially select two different sites of the Dy atom near the ac-3 step edge in Fig. 7(d) and then obtain two fully relaxed configurations in Figs. 7(e) and 7(f). Two geometries in Figs. 7(e) and 7(f) are different. The configuration in Fig. 7(e) has a higher chemical potential or binding energy $\mu = E_{\text{bind}} = -5.235 \text{ eV}$ than $\mu = E_{\text{bind}} = -5.964 \text{ eV}$ for that in Fig. 7(f).

C. TLG zz57 steps

In the zz57 step calculations, we first initially modify a zz-3 step in Fig. 6(d) into a zz57-3 step. After full relaxation,

we obtain the configuration in Fig. 8(a). Then we select three different sites of the Dy atom near the zz57-3 step edge in Fig. 8(a). Sequential full relaxations yield the three configurations in Figs. 8(b)–8(d) with $\mu = E_{\text{bind}} = -4.826, -4.108,$ and -4.820 eV , respectively. For Fig. 8(d), the initial position of the Dy atom is chosen to be beneath the TLG ribbon, but that for Fig. 8(b) or 8(c) is not.

D. An analysis for interactions between Dy and TLG steps

As defined in Eq. (B1), the chemical potential μ reflects the average interaction strength between one Dy atom and its surroundings. Lower (higher) μ corresponds to a stronger (weaker) interaction of a Dy atom with other atoms in a configuration on average. From Fig. 6 or Table S2 in the Supplemental Material [57], for the μ values, zz-1 is $\sim 1.5 \text{ eV}$ lower than zz-3, while zz-3 is $\sim 1.2 \text{ eV}$ lower than zz-3-c. Then an order of the interaction strength from strong to weak is $zz-1 > zz-3 > zz-3-c$. The strongest interaction for zz-1 is plausibly because the strip of exposed BLG between the two steps is narrow so that Dy can interact with both step edges. Plausibly, with increasing strip width, Dy should tend to interact with only one step, and therefore, the interaction would become weaker, as that for zz-3. Once a step is saturated by Dy, e.g., a Dy chain like zz-3-c in Fig. 6, the average interaction would become even further weakened. Similarly,

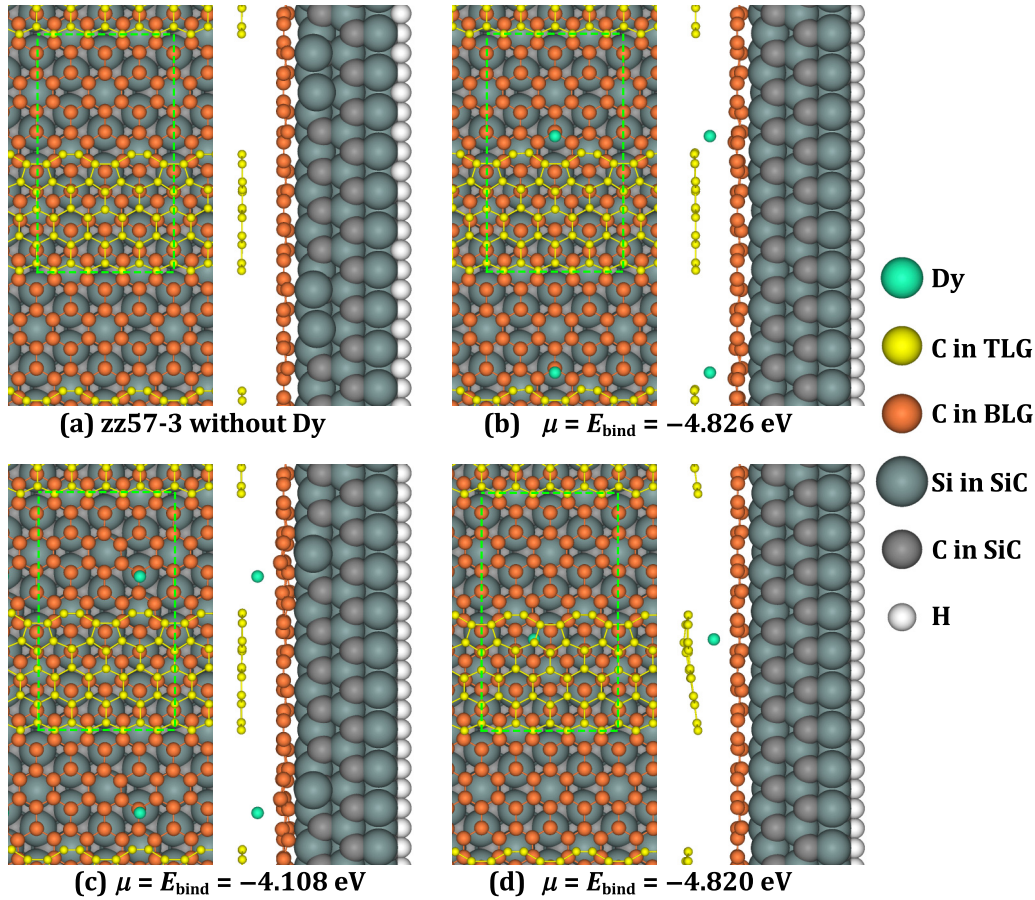


FIG. 8. Fully relaxed structures of the $zz57-3$ step with and without Dy atoms. The green dashed frame indicates the $2\sqrt{3}a_{\text{SiC}} \times 6a_{\text{SiC}}$ supercell used in our density functional theory (DFT) calculations. (a) Step $zz57-3$ is obtained by removing three zigzag rows and then relaxing. One of two steps is initially constructed by alternatively connecting C_5 and C_7 rings [31]. (b)–(d) Three configurations by relaxing one Dy atom at three different initial positions at the $zz57-3$ step. During energy minimization, except all relaxed atoms, the bottommost C and Si single-atom-thick layers are fixed. For (b)–(d), we also fix the lateral coordinates of four C atoms of the step edge without the Dy atom.

from ac-1 to ac-3 in Fig. 7 or Table S2 in the Supplemental Material [57], the interaction also becomes weaker with a drop of ~ 0.3 eV. This DFT result is instructive for understanding the intercalation of a Dy atom via a TLG step, as discussed in the next section.

In addition, by overall comparison of the μ values for zigzag ($zz-1$, $zz-3$, and $zz-3-c$), armchair ($ac-1$ and $ac-3$), and $zz57$ ($zz57-3$) steps in Figs. 6–8 or Table S2 in the Supplemental Material [57], an order from lower to higher chemical potential and therefore the average interaction from stronger to weaker is zigzag $>$ armchair $>$ $zz57$. This order is the same as that for Cu at graphite steps, where the stability order ($zz57 >$ armchair $>$ zigzag) of step-edge types is exactly opposite to the average interaction strength from stronger to weaker [31].

To search the global minimum of energy for Dy at a specific step edge, one should in principle relax a great number of configurations. However, it is often the case that the global minimum can be obtained by judiciously relaxing a limited number of initial configurations. Testing multiple configurations, we find that the Dy atom relaxes to the two or three configurations selected in Secs. V A–V C, i.e., analysis of these configurations suffices to determine the global minimum with the lowest μ (or E_{bind}) value for the Dy atom at each step in Figs. 6–8 with little uncertainty. Also, in contrast to

the whole energy landscape for a Dy atom at a TLG step of the graphene supported by SiC, the E_{bind} values of different configurations for each step in Figs. 6–8 have relatively small variations (significantly < 1 eV; see Table S2 in the Supplemental Material [57]), as discussed in the next section.

VI. ENERGY LANDSCAPE OF A SINGLE Dy ATOM NEARBY TLG STEPS

By determining E_{bind} values for a Dy atom on TLG, at various TLG steps, in the BT gallery, and in the BS gallery, we can plot a binding energy landscape. Any one black line in Fig. 9(a) corresponds to the lowest E_{bind} value (below, we always refer to this lowest value whenever E_{bind} is mentioned) from our DFT calculations in Sec. IV or V for a Dy atom at each of the above different positions. As already analyzed in Sec. IV, the thermodynamic favorability of a Dy atom on TLG, in the BT gallery, and in the BS gallery has the order of BT $>$ top $>$ BS. From Fig. 9(a), all E_{bind} values for various steps are lower than the value in the BT gallery. Therefore, the favorability order after considering these steps is updated as $zz-1 >$ $zz-3 >$ $ac-1 >$ $ac-3 >$ $zz57-3 >$ $zz-3-c >$ BT $>$ top $>$ BS, as indicated by the lines with the E_{bind} values from lower to higher in Fig. 9(a).

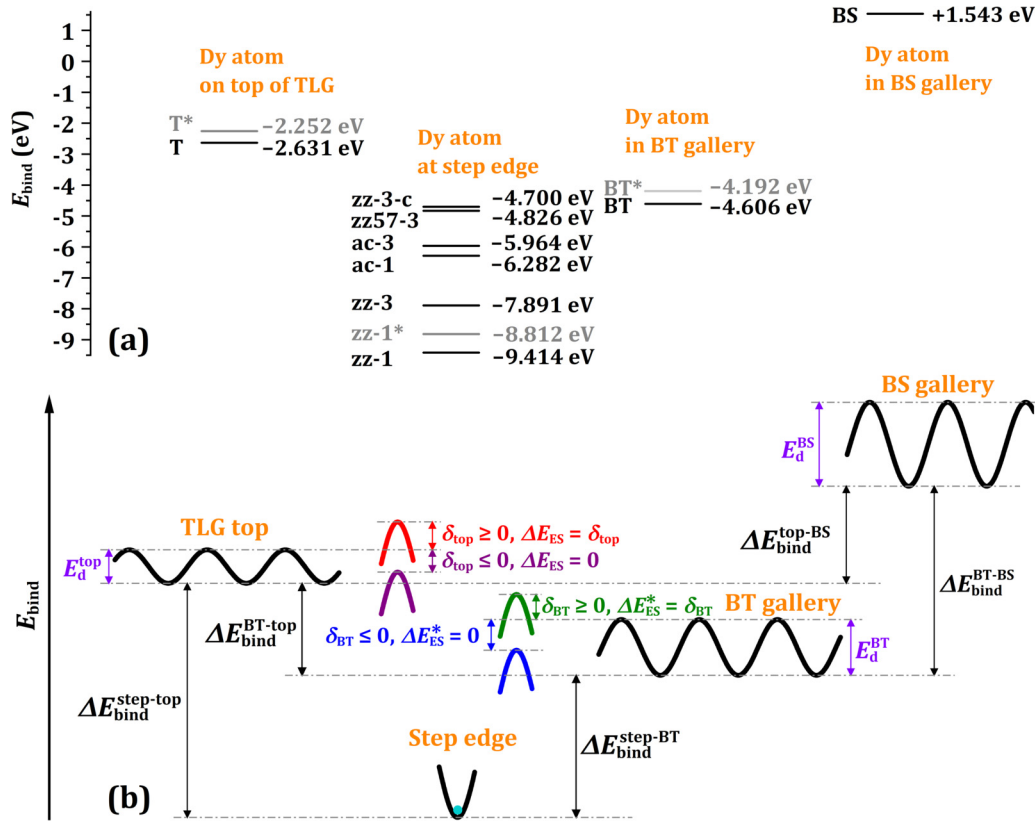


FIG. 9. (a) Binding energies (E_{bind}) of one Dy atom on top-layer graphene (TLG), at various step edges, in the gallery between buffer-layer graphene (BLG) and TLG (BT gallery), and in the gallery between BLG and the terminal Si layer (BS gallery). (b) Schematic of binding energy landscape for a guest atom (like a Dy atom) on TLG, at a step, in the BT gallery, and in the BS gallery. Various diffusion barriers and the binding energy differences are indicated. For more details, see text.

Given the E_{bind} values in Fig. 9(a), we can assess the kinetic process of a Dy atom from top terrace to a gallery via a step. Because E_{bind} of a Dy atom on TLG is $\sim 2-7$ eV higher than that at one type of step edge or ~ 1.6 eV higher than that in the BT gallery [Fig. 9(a)], there is a large thermodynamic driving force from the top terrace to a step edge or to the BT gallery. To conveniently analyze the kinetic process, we make a schematic of the energy landscape in Fig. 9(b) for any given guest atom (like a Dy atom) on TLG, at a step, in the BT gallery, and in the BS gallery. In Sec. IV, we have obtained the diffusion barrier $E_d^{\text{top}} = 0.446$ eV for the Dy atom on TLG. We also must consider that, for an atom crossing a step on a surface from upper to lower terrace, the atom generally needs to overcome an extra barrier, i.e., the Ehrlich-Schwobel (ES) barrier ΔE_{ES} , relative to the terrace diffusion barrier E_d^{top} . In principle, one can perform DFT-CINEB calculations to obtain ΔE_{ES} , but such calculations are highly demanding. Instead, we make a rough estimate as below.

Note that the ES barrier ΔE_{ES} for a metal atom crossing a step on a crystalline metal surface is usually $\lesssim 0.2$ eV [58–60]. In Fig. 9(b), we define an ES barrier parameter δ_{top} , which is the energy difference between the transition states of the guest atom at the step edge and at a TLG terrace position far from the step. If $\delta_{\text{top}} \geq 0$, $\Delta E_{\text{ES}} = \delta_{\text{top}}$, but if $\delta_{\text{top}} \leq 0$, $\Delta E_{\text{ES}} = 0$ [60]. See the red and purple curves in Fig. 9(b) for $\delta_{\text{top}} \geq 0$ and $\delta_{\text{top}} \leq 0$, respectively. For a Cu atom crossing

a graphite step edge, we estimated $\delta_{\text{top}} < 0$, and therefore, $\Delta E_{\text{ES}} = 0$ from our previous DFT calculations [31]. For a Dy atom on TLG, we expect that ΔE_{ES} for crossing a TLG step (also note that ΔE_{ES} can vary for different step types) is likely also $\lesssim 0.2$ eV, and this allows us to make a conservative estimate of $\Delta E_{\text{ES}} = 0.1$ eV with an error bar of $\sim \pm 0.1$ eV. Thus, the total barrier of the Dy atom crossing the step from upper to lower terrace is around $E_d^{\text{top}} + \Delta E_{\text{ES}} \approx 0.446 + 0.1 \approx 0.5$ eV, much less than the penetration barrier $E_{\text{dp}} \gtrsim 3.5$ eV (obtained in Sec. IV). Therefore, it is much easier that a Dy atom diffusing on TLG crosses the TLG step edge and then attaches to a step site on BLG than directly penetrating the TLG into the BT gallery.

Once a guest atom (like Dy) crosses the TLG step edge and then attaches to a step site on BLG, it can detach from the step and sequentially either return to the TLG terrace or intercalate into the BT gallery. For the detaching from the step site back to the TLG terrace, the energy barrier is $\Delta_{\text{back}} = \Delta E_{\text{bind}}^{\text{step-top}} + E_d^{\text{top}} + \Delta E_{\text{ES}}$, where $\Delta E_{\text{bind}}^{\text{step-top}}$ is the binding energy difference from a step edge to TLG terrace [see Fig. 9(b)]. For the detaching from a step site into the BT gallery, the energy barrier is $\Delta_{\text{in}} = \Delta E_{\text{bind}}^{\text{step-BT}} + E_d^{\text{BT}} + \Delta E_{\text{ES}}^*$, where $\Delta E_{\text{bind}}^{\text{step-BT}}$ is the binding energy difference from the step site to the BT gallery, E_d^{BT} is the diffusion barrier in the BT gallery, and $\Delta E_{\text{ES}}^* \geq 0$ is defined as an ES-like intercalation barrier parameter (see Appendix C). The corresponding rates

for the above two detachment processes are determined by the Arrhenius forms $r_{\text{back}} = \nu e^{-\beta \Delta_{\text{back}}}$ (back to top) and $r_{\text{in}} = \nu e^{-\beta \Delta_{\text{in}}}$ (into the BT gallery).

For a Dy atom, $E_{\text{d}}^{\text{top}} + \Delta E_{\text{ES}} \approx 0.5 \text{ eV}$ (as analyzed above), and $\Delta E_{\text{bind}}^{\text{step-top}}$ is in a range of 2–7 eV for different types of step [see Fig. 9(a)]. Correspondingly, $\Delta_{\text{back}} = \Delta E_{\text{bind}}^{\text{step-top}} + E_{\text{d}}^{\text{top}} + \Delta E_{\text{ES}}$ is in a range of $\sim 2.5\text{--}7.5 \text{ eV}$. The large Δ_{back} effectively inhibits the detachment from the step site back to the TLG terrace, e.g., $r_{\text{back}} = \nu e^{-\beta \Delta_{\text{back}}} \approx 2.5/\text{s}$ is rather low at $T = 1000 \text{ K}$, even for the lower limit 2.5 eV [i.e., for zz-3-c step; see Fig. 9(a)] of Δ_{back} .

Let us also analyze r_{in} . For a Dy atom, $E_{\text{d}}^{\text{BT}} = 0.535 \text{ eV}$ (obtained in Sec. IV), and we can ignore ΔE_{ES}^* (see Appendix C), while $\Delta E_{\text{bind}}^{\text{step-BT}}$ is in a range of $\sim 0.1\text{--}4.8 \text{ eV}$ for different types of step [see Fig. 9(a)]. Then $\Delta_{\text{in}} = \Delta E_{\text{bind}}^{\text{step-BT}} + E_{\text{d}}^{\text{BT}} + \Delta E_{\text{ES}}^*$ is in a range of $\sim 0.6\text{--}5.3 \text{ eV}$. For the upper limit 5.3 eV (i.e., for zz-1 step) of Δ_{in} , the rate $r_{\text{in}} = \nu e^{-\beta \Delta_{\text{in}}} \approx 0$ at $T = 1000 \text{ K}$, indicating that the detachment from the zz-1 step into the BT gallery is inhibited. However, for the lower limit 0.6 eV (i.e., for zz-3-c step) of Δ_{in} , the rate $r_{\text{in}} = \nu e^{-\beta \Delta_{\text{in}}} \approx 10^{10}/\text{s}$ at $T = 1000 \text{ K}$, indicating that the detachment from a zz-3-c step into the BT gallery is much easier. Similar analyses at other temperatures and for other step types can be straightforward. Therefore, the binding energy difference $\Delta E_{\text{bind}}^{\text{step-BT}}$ from the step edge to the BT gallery is the main factor determining the ease or difficulty of Dy atom intercalation into the BT gallery. Thus, detachment of a Dy atom from a step edge to the BT gallery varies from easiest to most difficult in the order zz-3-c, zz57-3, ac-3, ac-1, zz3, and zz1, corresponding to the $\Delta E_{\text{bind}}^{\text{step-BT}}$ values varying from smallest to largest in Fig. 9(a).

VII. ADSORPTION AND INTERCALATION OF Dy WITH HIGHER COVERAGES

In experiments [37], the coverage of Dy for either adsorption or intercalation is often $\gg \frac{1}{16} \text{ ML}$ described in Sec. IV. Thus, we also choose two higher coverages of $\frac{1}{4}$ and 1 ML to assess the energetics of Dy adsorption and intercalation in this section. In our DFT calculations for these higher coverages, we use the same supercell and k mesh as those in Sec. IV, and therefore, the coverages $\frac{1}{4}$ and 1 ML correspond to 4 and 16 Dy atoms in the supercell, respectively.

A. $\frac{1}{4} \text{ ML Dy}$

We first analyze Dy adsorption with two different configurations, one uniformly distributed and the other clustered, the corresponding fully relaxed configurations being shown in Figs. 10(a) and 10(b), respectively. The chemical potential μ of the clustered configuration in Fig. 10(b) is 0.465 eV lower than the uniform configuration in Fig. 10(a). This seems to indicate that the Dy on the TLG tends to clustering instead of a uniform layer for this coverage.

For the intercalation in the BT gallery, we select one uniform configuration. After full relaxation, the configuration is shown in Fig. 10(c) with a significantly lower μ by $\sim 2 \text{ eV}$ than for adsorption. Thus, the intercalation for $\frac{1}{4} \text{ ML Dy}$ into the BT gallery is much more favorable than the adsorption,

and then consistent with the results for $\frac{1}{16} \text{ ML Dy}$ approximately representing an isolated Dy atom (see Fig. 3 and Table S1 in the Supplemental Material [57]).

For the intercalation in the BS gallery, we also select one uniform configuration, as fully relaxed in Fig. 10(d). The μ value of this configuration is only 0.520 eV higher than in the BT gallery, but significantly lower by $\sim 1.5 \text{ eV}$ than the adsorption. Thus, the intercalation for $\frac{1}{4} \text{ ML Dy}$ into the BS gallery is slightly more unfavorable than in the BT gallery but becomes significantly more favorable than adsorption, in contrast to the results for $\frac{1}{16} \text{ ML Dy}$ (see Fig. 3 and Table S1 in the Supplemental Material [57]), where the Dy atom in BS gallery is most unfavorable.

For the above analysis, here, it is necessary to mention some caveats. These caveats also apply for the 1 ML calculations in the next subsection (Sec. VII B).

(i) To judge the relative favorability of the configurations, we use μ . This is equivalent to using total energy E_{tot} [see Eq. (B1)] for systems with the same Dy coverage. μ cannot be used to judge the relative favorability of the configurations with different Dy coverages.

(ii) Higher (lower) μ for the same Dy coverage corresponds to a less (more) favorable configuration with a stronger (weaker) interaction per Dy atom with other atoms (see Appendix B). Thus, for a coverage of $\frac{1}{4} \text{ ML}$, the favorability order of BT > BS > top is equivalent to the order of interaction strength from stronger to weaker (also see Sec. VII C).

(iii) For calculations of adsorption on TLG, intercalation in the BT gallery, and intercalation in the BS gallery, we only relax two, one, and one configuration, respectively. This does not guarantee that we identify the global-energy-minimum configuration for any of these three cases. Finding the global energy minimum needs performance of DFT calculations with as many different selected initial configurations as possible (this is of course extremely expensive computationally). However, we believe that the above-selected calculations are sufficient to ensure that each configuration is at least close to the global energy minimum, considering that the μ values of two configurations in Figs. 10(a) and 10(b) have a difference $< 0.5 \text{ eV}$. The sufficiently small difference (e.g., significantly $< 1 \text{ eV}$) in μ does not affect the above favorability order.

(iv) The fully relaxed configurations in Figs. 10(a) and 10(b) with Dy on TLG do not change the AB stacking between TLG and BLG, but the configuration in Fig. 10(c) with Dy in the BT gallery produces AA-like stacking, while the configuration in Fig. 10(d) with Dy in the BS gallery produces neither AA nor AB stacking. At least for finite graphene regions with free boundaries, a stacking change can occur after intercalation in experiments [53–56]. A large graphene layer could probably change local stacking and eventually convert the entire layer (e.g., see Fig. 2). For a discussion of stacking effects in our DFT calculations, see Appendix D.

B. 1 ML Dy

For 1 ML Dy adsorption, we initially put one Dy single-atom-thick layer (i.e., 16 Dy atoms per cell) on TLG with each Dy atom at the center site of a C_6 ring. After full relaxation, the initial Dy layer becomes two Dy layers, as indicated by eight smaller (upper) and eight larger (lower)

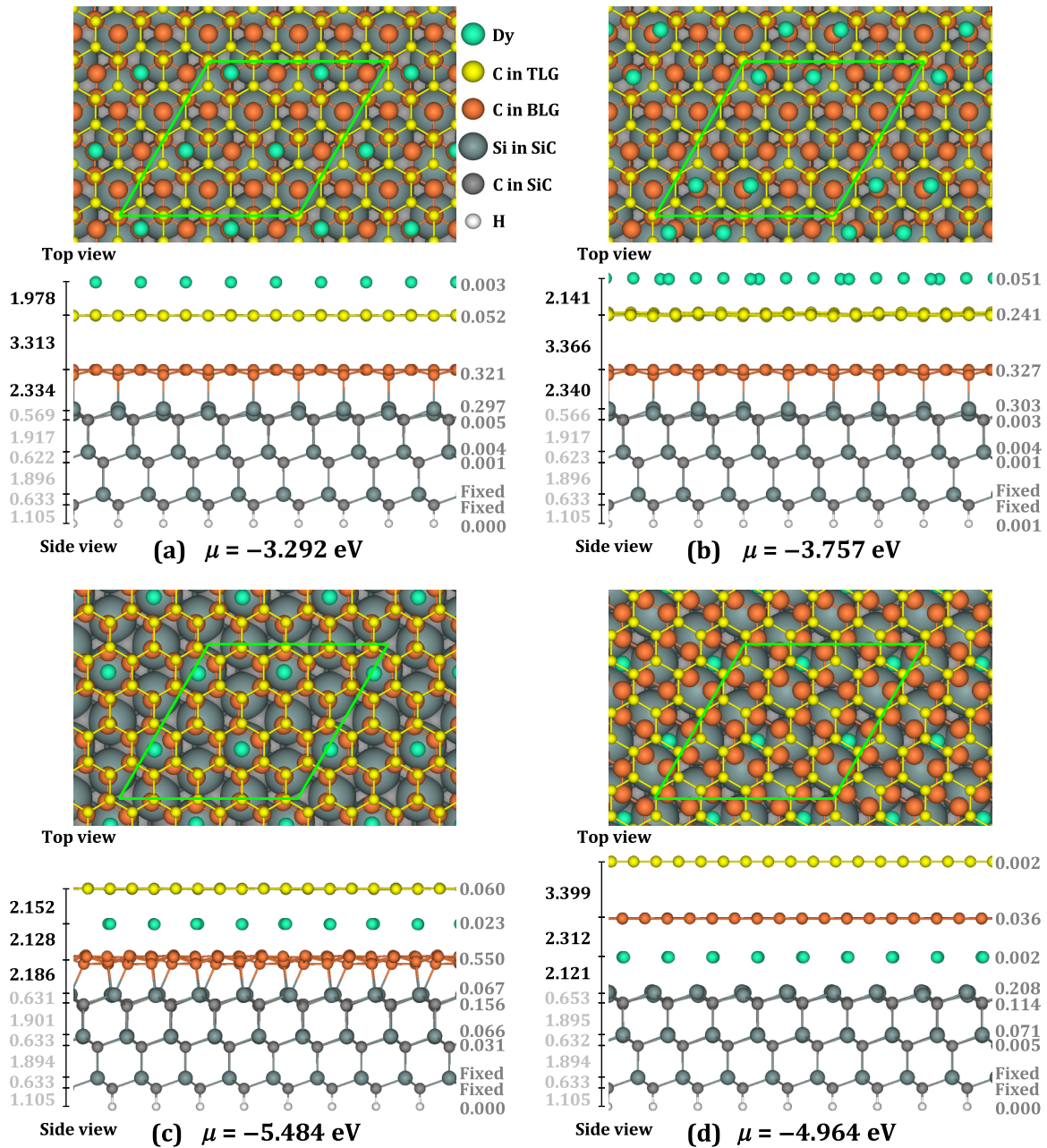


FIG. 10. Fully relaxed structures with a Dy coverage of $\frac{1}{4}$ monolayer (ML) (a) and (b) on top-layer graphene (TLG), (c) in the gallery between buffer-layer graphene (BLG) and TLG (BT gallery), and (d) in the gallery between BLG and the terminal Si layer (BS gallery) from our density functional theory (DFT) calculations. The four Dy atoms in the $2\sqrt{3}a_{\text{SiC}} \times 2\sqrt{3}a_{\text{SiC}}$ supercell (green frame in top view) are always initially set to be uniformly distributed, except for (b), where the nearest-neighbor distance between two Dy atoms is reduced to half of that for (a). The left of the side view shows the interlayer spacings (in angstroms), and the right shows the corrugations (in angstroms) for each single-atom-thick layer.

green balls per cell in Fig. 11(a). Similarly, full relaxation for the initial Dy layer in the BT gallery also yields two Dy layers [see Fig. 11(b)], but the upper Dy layer and the lower Dy layer contain 12 and 4 atoms per cell, respectively. The full relaxation for the initial Dy layer in the BS gallery yields two Dy layers [see Fig. 11(c)] with the upper Dy layer and the lower Dy layer containing 7 and 9 atoms per cell, respectively.

In Fig. 11, the μ values have a decreasing order of BT (-4.132 eV) > top (-4.202 eV) > BS (-4.790 eV), and therefore, the favorability order is BT < top < BS, which is

opposite to the order for $\frac{1}{16}$ ML Dy (see Fig. 3 and Table S1 in the Supplemental Material [57]). However, these three μ values are close to each other (within 0.7 eV). In addition, it is also possible that these configurations do not correspond to the global energy minima [e.g., the configuration in Fig. 11(b) is perhaps not the global energy minima which probably has a 0.7 eV lower μ value], as noted in Sec. VII A. Again, search for the global energy minima is computationally expensive and is not implemented in this paper. Despite this uncertainty,

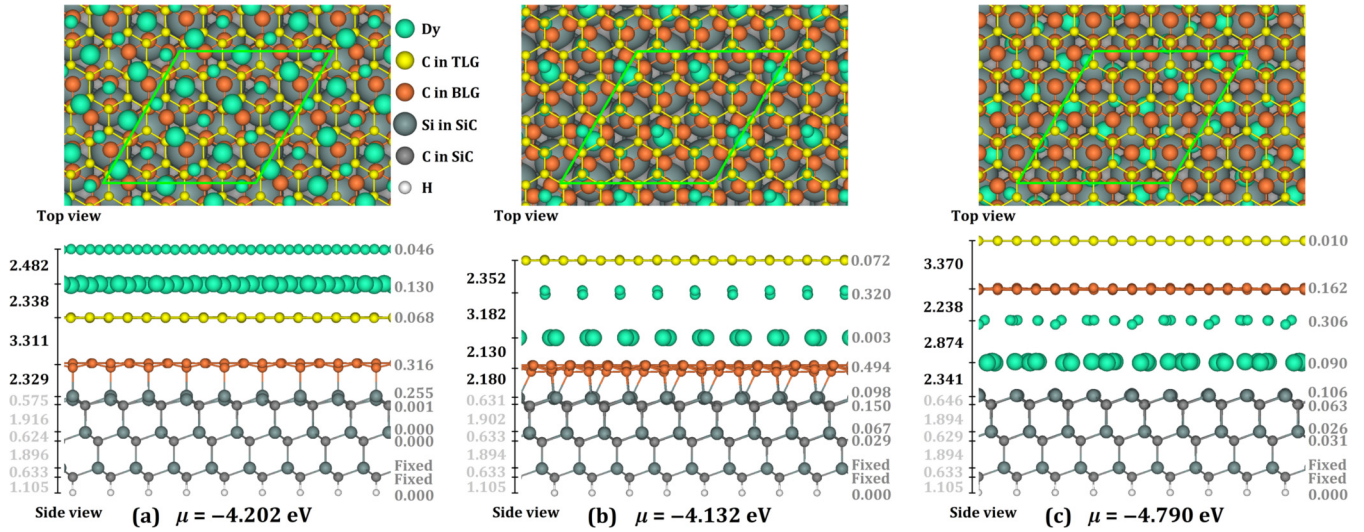


FIG. 11. Fully relaxed structures with a Dy coverage of 1 monolayer (ML) (a) on top-layer graphene (TLG), (b) in the gallery between buffer-layer graphene (BLG) and TLG (BT gallery), and (c) in the gallery between BLG and the terminal Si layer (BS gallery) from our density functional theory (DFT) calculations. The 16 Dy atoms in the $2\sqrt{3}a_{\text{SiC}} \times 2\sqrt{3}a_{\text{SiC}}$ supercell (green frame in top view) are always initially set to be uniformly distributed. After full relaxation, the Dy single-atom-thick layer for any initial structure becomes two single-atom-thick layers, as indicated by small and large balls for Dy. The left of the side view shows the interlayer spacings (in angstroms), and the right shows the corrugations (in angstroms) for each single-atom-thick layer.

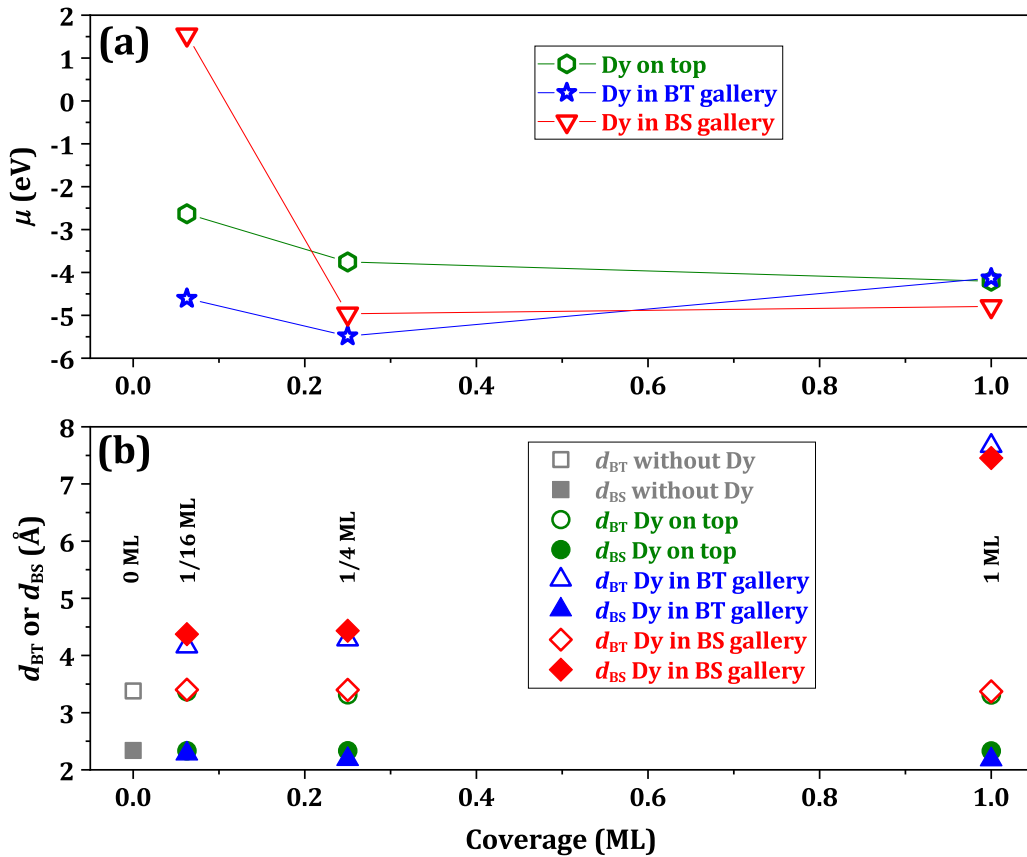


FIG. 12. Coverage dependences of (a) chemical potential (μ) and (b) interlayer spacings (d_{BT} and d_{BS}) without or with Dy on top-layer graphene (TLG), in the gallery between buffer-layer graphene (BLG) and TLG (BT gallery), and in the gallery between BLG and the terminal Si layer (BS gallery). Density functional theory (DFT) data in (a) and (b) are from Table S1 in the Supplemental Material [57] and Table I, respectively.

TABLE II. Bulk properties of 6H-SiC, graphite, graphene, and hcp Dy from our DFT calculations compared with available experimental values. a or c is the lattice constant. B_0 and B'_0 are the bulk modulus and the first derivative of the bulk modulus with respect to pressure, respectively. The cohesive energy is $E_{\text{coh}} = E_{\text{gas}} - \sigma_{\text{bulk}}$, where E_{gas} is the energy of a single atom in its gas phase, and σ_{bulk} is the energy per atom in its bulk phase.

System	Method	a (Å)	c (Å)	B_0 (GPa)	B'_0	E_{coh} (eV)
6H-SiC	DFT, optB88-vdW	3.09545	15.19541	212.2	5.4	
	experiments	3.08129 ^a	15.11976 ^a			
		3.0810 ^b	15.1248 ^b	230.2 ^c	4 ^c	
				221 ^d		
Graphite	DFT, optB88-vdW	2.465 ^e	6.701 ^e			7.800 ^e
	experiments	2.4589 ^f	6.6720 ^g			7.37 ^h
Graphene	DFT, optB88-vdW	2.464 ^e				7.730 ^e
	experiment	2.4 ⁱ				
hcp Dy	DFT, PBE	3.620	5.625			4.20
	DFT, optB88-vdW	3.568	5.575			4.31
	experiments	3.584 ^j	5.668 ^j			
		3.59 ^f	5.65 ^f			3.04 ^f
						3.12 ^k

^aReference [63].

^bReference [64].

^cReference [65].

^dCalculated from elastic stiffness coefficients C_{ij} [66] using the data in Ref. [67].

^eReference [41].

^fAt 78 to 298 K [68].

^gAt 4.2 K [68].

^hReference [69].

ⁱReference [70].

^jReference [71].

^kReference [72].

the three configurations in Fig. 11 for 1 ML, together with the configurations in Fig. 10 for $\frac{1}{4}$ ML, can provide an instructive comparative guide for assessing the coverage dependences, as discussed below.

C. Coverage dependences of chemical potentials and interlayer spacings

Figure 12(a) summarizes our DFT predictions for the variation of μ values with Dy coverage ($\frac{1}{16}$, $\frac{1}{4}$, and 1 ML). For $\frac{1}{16}$ ML, the favorability order of Dy is BT > top > BS with significantly larger increments (~ 2.0 to 5.0 eV) in μ . For $\frac{1}{4}$ ML, the order is BT > BS > top with intermediate increments (~ 0.5 to 1.7 eV) in μ , i.e., the intercalation into the BS gallery becomes much more favorable than adsorption on TLG, in contrast to $\frac{1}{16}$ ML, where approximately a single Dy atom is much more unfavorable for the intercalation into the BS gallery. For 1 ML, the order is BS > top > BT with small increments (~ 0.07 to 0.66 eV) in μ , i.e., becomes opposite in contrast to $\frac{1}{16}$ ML, although this order has an uncertainty, as mentioned in Sec. VII B. In addition, from the Fig. 12(a), with increasing coverage of Dy from one to two layers, the μ value naturally approaches $-E_{\text{coh}} = -4.31$ eV for hcp Dy bulk (Table II), indicating the self-consistency of our DFT calculations.

In Fig. 12(b), we summarize the coverage dependence of interlayer spacings d_{BT} and d_{BS} . The data for all interlayer spacings and corrugations are shown in Figs. 4, 10, and 11

(also see Table I). From Fig. 12(b), any spacing without Dy intercalated has almost no change for any coverage relative to 0 ML (i.e., without Dy). After a gallery is intercalated, the spacing significantly increases (see the values highlighted by the bold fonts in Table I). Here, d_{BT} and d_{BS} increase by $\sim 23\%$ and 87% (27% and 90%) for $\frac{1}{16}$ ($\frac{1}{4}$) ML, respectively. For 1 ML, Dy becomes two layers, and thus, d_{BT} and d_{BS} increase even larger, by $\sim 127\%$ and 219% , respectively. In addition, we emphasize that, from Figs. 4, 10, and 11, the corrugations of layers near the intercalated Dy for any coverages are generally larger with different degrees relative to the farther layers. A larger (smaller) corrugation reflects a larger (smaller) standard error of the interlayer spacing, which is an average value, as defined in the caption in Fig. 1.

Next, we make a brief qualitative analysis for the relationship between interlayer spacings with intercalated Dy and the corresponding chemical potentials. For a low coverage of Dy, e.g., $\frac{1}{16}$ or $\frac{1}{4}$ ML, d_{BS} increases by $\sim 87\%$ or 90% after the Dy intercalation, while d_{BT} increases by only $\sim 23\%$ or 27% , respectively. As in our previous analysis for the intercalation of a guest atom into multilayer graphene [43], the total energy (or equivalently the chemical potential) can be decomposed into two components. One is the elastic contribution (positive) due to the relaxation of C atoms (i.e., the displacements from equilibrium positions of C atoms) near the intercalated guest atom, reflected by relaxing to a specific interlayer spacing with the corrugations (including protrusions or local bending with strain). Another contribution (negative) is the electronic

effect not related to the relaxation, reflected by the interactions between atoms.

For low coverages ($\frac{1}{16}$ or $\frac{1}{4}$ ML), we assume that the electronic contributions do not significantly differ (or do not dominate) for the intercalation in the BT or BS gallery and assume that a larger (smaller) incremental change in interlayer spacing approximately corresponds to larger (smaller) intercalation-induced strain. Then the elastic contributions dominate the chemical potentials: a larger (smaller) incremental change in interlayer spacing [and therefore larger (smaller) elastic contribution] corresponds to a higher (lower) chemical potential. For $\frac{1}{16}$ ML, $d_{BS} = 4.374 \text{ \AA}$ has a larger incremental change of $\sim 87\%$ with a higher $\mu = +1.543 \text{ eV}$, while $d_{BT} = 4.156 \text{ \AA}$ has a smaller incremental change of only $\sim 23\%$ with a lower $\mu = -4.606 \text{ eV}$. Similarly, for $\frac{1}{4}$ ML, $d_{BS} = 4.433 \text{ \AA}$ has a larger incremental change of $\sim 90\%$ with a higher $\mu = -4.964 \text{ eV}$, while $d_{BT} = 4.280 \text{ \AA}$ has a smaller incremental change of only $\sim 27\%$ with a lower $\mu = -5.484 \text{ eV}$. This result is consistent with the above elastic-contribution-dominant assumption.

For the high coverage (1 ML), after intercalation, $d_{BS} = 7.453 \text{ \AA}$ has a larger incremental change of $\sim 219\%$ but with a lower $\mu = -4.790 \text{ eV}$, while $d_{BT} = 7.665 \text{ \AA}$ has a smaller incremental change of $\sim 127\%$ but with a higher $\mu = -4.132 \text{ eV}$. This result is opposite to that for the above low coverages. A surmise is that the electronic contributions would be dominant over the elastic contributions for a high Dy coverage. In general, a higher Dy coverage corresponds to more nearest-neighbor interactions between Dy atoms, and consequently, the electronic contributions increase. On the other hand, the bending with strain in graphene layers (and therefore elastic contributions) does not significantly increase for a sufficiently large interlayer spacing, which is mainly from a large translational shift between upper and lower parts of a gallery after the gallery is intercalated [see Figs. 11(b) and 11(c)].

VIII. CONCLUSIONS

We have performed first-principles DFT calculations for Dy adsorption and intercalation for a graphene-SiC system. From a chemical-potential analysis, we find that a single Dy atom intercalated into the BT gallery is $\sim 2 \text{ eV}$ more favorable than adsorption on TLG, and $>6 \text{ eV}$ more favorable than intercalated into the BS gallery. We also find that the direct penetration of a single Dy atom from the graphene top into the BT gallery is strongly inhibited with a large global barrier above 3.5 eV . In addition, we also obtain the diffusion barriers ~ 0.45 and 0.54 eV for a single Dy atom diffusing on TLG and in the BT gallery, respectively. We demonstrate that one Dy atom on TLG terrace can easily intercalate into the BT gallery by crossing specific types of TLG steps, e.g., a zz step presaturated by a Dy chain, or a $zz57$ step, at which the chemical potential of Dy is comparable to (vs much lower than) that in the BT gallery. Our DFT calculations for different Dy coverages (0 , $\frac{1}{16}$, $\frac{1}{4}$, and 1 ML) show that the preferred bonding location of Dy and the corresponding interlayer spacing for an intercalated gallery is coverage dependent, but the interlayer spacing for any unintercalated gallery almost does not depend on the coverage. These theoretical predictions

can be generally informative and instructive for studies of a graphene-SiC system intercalated by guest atoms.

ACKNOWLEDGMENTS

This paper was supported mainly by the US Department of Energy (DOE), Office of Science, Basic Energy Sciences, Materials Sciences and Engineering Division. This includes the contributions by Y.H. and M.C.T. Work by J.W.E. was supported by National Science Foundation Grant No. CHE-1507223. Research was performed at the Ames Laboratory, which is operated by Iowa State University under Contract No. DE-AC02-07CH11358. DFT calculations were mainly performed with a grant of computer time at the National Energy Research Scientific Computing Centre (NERSC). NERSC is a DOE Office of Science User Facility supported by the Office of Science of the US DOE under Contract No. DE-AC02-05CH11231. The calculations also partly used the Extreme Science and Engineering Discovery Environment (XSEDE), which is supported by the National Science Foundation under Grant No. ACI-1548562.

APPENDIX A: DFT BENCHMARK ANALYSIS FOR BULK PROPERTIES OF 6H-SiC, GRAPHITE, GRAPHENE, AND HCP Dy

To calculate the bulk properties of 6H-SiC, we use a conventional unit cell with a hexagonal structure of ABCACB stacking containing 6 C atoms and 6 Si atoms, as illustrated in Fig. 13. The k mesh is taken to be $51 \times 51 \times 13$, and the cutoff energy is set to be 557 eV , which is significantly larger than the VASP default value 400.000 eV for C (as well as 245.345 eV for Si), to guarantee the high accuracy of the DFT calculations. As listed in Table II, the lattice constants a and c of 6H-SiC from our optB88-vdW calculations are in good

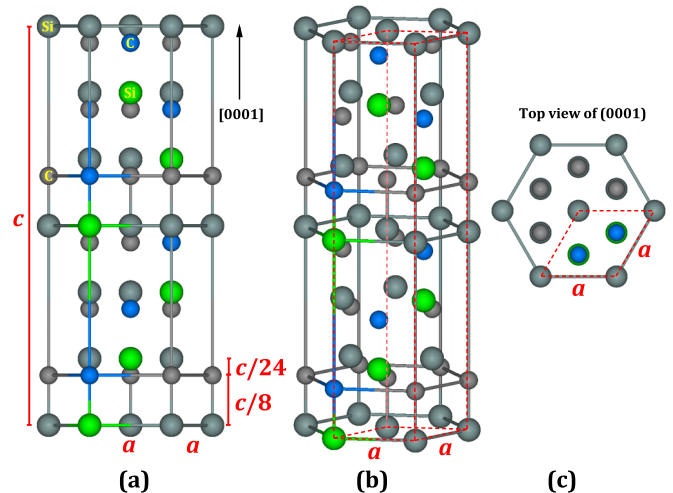


FIG. 13. The hexagonal cell of bulk 6H-SiC. (a) Side view of the (0001) plane. (b) A view inclined to the (0001) plane at an angle of 10° . (c) Top view of the (0001) plane. The dashed red frame indicates the unit cell used in our density functional theory (DFT) calculation for lattice constants a and c . The unit cell contains six C atoms (blue) and six Si atoms (green). Two different interlayer spacings $c/24$ and $c/8$ are also indicated [63].

agreement with experimental values. In the calculations for the lattice constants, we fully relax cell volume and shape as well as coordinates of all atoms to obtain a configuration with energy E_0 and corresponding volume V_0 . Then we calculate the energies of a series of configurations with volumes fixed around V_0 by relaxing cell shape to ensure that E_0 is the global energy minimum. Using the Birch-Murnaghan equation [61,62], we fit the data points of energy vs volume and obtain the bulk modulus B_0 and the first derivative B'_0 of the bulk modulus with respect to pressure. As listed in Table II, the B_0 and B'_0 of 6H-SiC from our optB88-vdW calculations are also in good agreement with experimental values.

As mentioned in Sec. II, the properties (including lattice parameters, cohesive energies, surface energies, step edge energies, graphene vacancy formation energies, etc.) of graphite and graphene from the optB88-vdW calculations can reproduce well the experimental data [41,31]. To be convenient, in Table II, we also list the lattice constants and cohesive energies of graphite and graphene from our previous optB88-vdW calculations [41] with the experimental values for comparison.

For hcp Dy, we use the primitive cell containing two Dy atoms. The k mesh is taken to be $51 \times 51 \times 51$, and the cutoff energy is 400 eV, which is much larger than the VASP default value 155.713 eV for Dy. This again guarantees the high computational accuracy. From Table II, the lattice constants a and c from our optB88-vdW calculations (as well as from our PBE calculations as a comparison) can be in good agreement with the experimental values, but the DFT cohesive energies (E_{coh}) have significant deviations away from the experimental values. The relatively large deviations in E_{coh} could be likely from the use of the pseudopotential (Dy_3 POTCAR) with 4*f* electrons frozen in the core. However, this is a standard pseudopotential model for the treatment of localized *f* electrons and has already been widely applied (see, e.g., Ref. [73]) because treating the electrons in the *f* orbital outside the core can give rise to unreliable behavior, e.g., the energy divergence during relaxation. Although this pseudopotential cannot reproduce experimental E_{coh} well, we assume that the contributions from 4*f* valence electrons to total energies would be largely cancelled when comparing relative energy differences for our surface systems in this paper.

APPENDIX B: FORMULATION OF CHEMICAL POTENTIAL, ADSORPTION ENERGY, BINDING ENERGY, COMBINATION ENERGY, AND INTERCALATION ENERGY

To assess the relative stability and the average strength of atom interactions of various structures involving Dy binding with the graphene-SiC system, particularly at step edges, we define a chemical potential of Dy as [31,28]

$$\mu = \frac{E_{\text{tot}} - E_{\text{cln}}}{n} - E_{\text{gas}}, \quad (\text{B1})$$

where E_{tot} is the total energy of the Dy structure plus graphene and SiC, E_{cln} is the energy of the fully relaxed clean graphene-SiC system (without Dy) with or without steps, n is the total number of Dy atoms in a supercell, and E_{gas} is the energy of one Dy atom in the gas phase. The chemical potential μ in Eq. (B1) accounts for the average strength of one Dy

atom interacting with its surroundings. A lower (higher) μ value corresponds to a configuration with a stronger (weaker) interaction of a Dy atom with other atoms on average. For one adatom ($n = 1$) adsorbed on TLG of the graphene-SiC system, μ reduces to the conventional adsorption energy

$$E_{\text{ads}} = E_{\text{tot}} - E_{\text{cln}} - E_{\text{gas}}. \quad (\text{B2})$$

To provide additional insight into the energy landscape of one specific Dy atom bound to different sites on the TLG ribbon, at a TLG step edge (with or without a Dy chain), and in the BT gallery, we also define a binding energy for this Dy atom as [31]

$$E_{\text{bind}} = E_{\text{tot}} - E_{\text{cln}}^* - E_{\text{gas}}, \quad (\text{B3})$$

where E_{cln}^* is the energy of the fully relaxed graphene-SiC system with or without a predecorated Dy chain. Lower E_{bind} indicates stronger binding between the Dy atom and other atoms. For the graphene-SiC system not predecorated by a Dy chain, E_{cln}^* reduces to E_{cln} , and then Eq. (B3) reduces to the case of $n = 1$ in Eq. (B1). In this case, $E_{\text{bind}} = \mu$.

Note that the energy reference in Eqs. (B1)–(B3) is E_{gas} . Here, we also define a combination energy [43]

$$E_{\text{comb}} = E_{\text{tot}} - E_{\text{cln}} - \sigma_{\text{bulk}}, \quad (\text{B4})$$

where σ_{bulk} is the energy per Dy atom in hcp Dy bulk crystal, instead of E_{gas} . Then E_{comb} quantifies the energy required for a Dy atom to become combined with the graphene-SiC system (e.g., adsorbed on TLG, bound at a step edge, or intercalated into a gallery), starting from hcp Dy bulk. Note that the difference $E_{\text{comb}} - \mu$ is equal to the cohesive energy $E_{\text{coh}} = E_{\text{gas}} - \sigma_{\text{bulk}}$ of hcp Dy bulk. For the case of intercalation, E_{comb} is often called the intercalation energy E_{int} [42]. From Eq. (B4), $E_{\text{comb}} > 0$ indicates that the combination of a Dy atom with the graphene-SiC system from hcp Dy bulk is endothermic, while $E_{\text{comb}} < 0$ indicates that the combination is exothermic.

APPENDIX C: ESTIMATE OF INTERCALATION BARRIER PARAMETER ΔE_{ES}^*

The ES-like intercalation barrier parameter ΔE_{ES}^* is defined as the energy difference between the transition states of the guest atom at a step edge and at a position (far from steps) in the BT gallery. The value of ΔE_{ES}^* depends on the type of the step edge. In principle, one can obtain ΔE_{ES}^* by calculating the MEP for the guest atom crossing the step edge, e.g., using the CINEB method with two endpoints at the configurations in Figs. 6(h) and 6(i) for the zz-3-c step or in Figs. 8(b) and 8(d) for the zz57 step. Unfortunately, such CINEB calculations are computationally highly demanding and not implemented in this paper. Instead, we can make a reasonable estimate for different types of step. Like the definitions of δ_{top} and ΔE_{ES} , we can also define δ_{BT} satisfying $\Delta E_{\text{ES}} = \delta_{\text{BT}}$ for $\delta_{\text{BT}} \geq 0$, but $\Delta E_{\text{ES}} = 0$ for $\delta_{\text{BT}} \leq 0$, corresponding to the green or blue curves in Fig. 9(b), respectively. For zz-1, zz-3, ac-1, or ac-3 with a lower E_{bind} [as in Fig. 9(a)], we expect that the δ_{BT} value would be < 0 because there seems to be a sharp energy gradient from the step edge to the BT gallery (a similar picture to a Pb atom diffusing on an inversely stepped Pb(111) nanofilm from a region with lower adsorption energy to the

adjacent region with significantly higher adsorption energy by crossing an underlying buried step [60]; also see Sec. S3 [57]). For zz-3-c or zz57-3 with a higher E_{bind} [relatively closer to the E_{bind} value in BT gallery, as in Fig. 9(a)], the energy gradient from the step edge to the BT gallery becomes less sharp (e.g., the E_{bind} value increases by only ~ 0.19 eV from Figs. 6(h) to 6(i) for the zz-3-c step or by ~ 0.01 eV from Figs. 8(b) to 8(d) for the zz57 step, cf. an increase of ~ 4.5 eV for the zigzag step in Sec. S3 in the Supplemental Material [57]). Therefore, the δ_{BT} value for zz-3-c or zz57-3 would be >0 . It follows that ΔE_{ES}^* would be nonzero, but likely has a comparable value with ΔE_{ES} , which is usually $\ll 1$ eV, as analyzed in Sec. VI.

APPENDIX D: STACKING EFFECTS ON DFT RESULTS

As noted in Tables S1 and S2 in the Supplemental Material [57], when all coordinates of C atoms in the TLG (or a TLG ribbon) for a configuration are relaxed during the structure optimization, the TLG sometimes can have a shift so that the initial AB stacking between TLG and BLG finally becomes AA or AC stacking or an intermediate stacking between two of AA, AB, and AC. As mentioned in Sec. VII A, the stacking changes with domain boundaries or with intercalation can be possible in experimental observations, but it could be also a possible artificial effect when one uses a finite supercell size

to simulate an infinite system with perfect graphene layers in DFT calculations. This artificial effect cannot be cancelled, especially when one compares the energies of two configurations with and without stacking change, respectively, so that an error is created.

To estimate such errors, we performed two DFT calculations for AB and AA stacking of freestanding bilayer graphene using the $a_{\text{C}} \times a_{\text{C}}$ unit cell (containing 4 C atoms) with a k mesh of $41 \times 41 \times 1$. Also note that AB stacking is equivalent to AC stacking for bilayer graphene. From our DFT calculations, the AB stacking is energetically more favorable than AA stacking with an energy difference of 0.01983 eV per unit cell. Then for an $ma_{\text{C}} \times na_{\text{C}}$ supercell, there will be an error of $0.01983 \text{ eV} \times mn$ in total energy when two configurations with AB and AA stacking are used to calculate the energetic quantities in Eqs. (B1) to (B4). Thus, for the results (in Table S1 in the Supplemental Material [57]) with stacking changes (including the intermediate stacking between AB and AA), where a $4a_{\text{C}}^* \times 4a_{\text{C}}^*$ supercell is used, the errors should be within about $0.01983 \times 16 \approx 0.3$ eV, which is sufficiently small relatively and clearly does not affect our conclusions. Relative to Fig. 7(a) without the Dy atom or Fig. 7(b) with the Dy atom, the TLG ribbon in Fig. 7(c) has a shift. In this case, the TLG ribbon size is $4a_{\text{C}}^* \times 5a_{\text{C}}^*$, and then the error should be estimated to be within about $0.01983 \times 20 \approx 0.4$ eV, which is also sufficiently small relatively and does not affect our conclusions.

-
- [1] M. S. Stark, K. L. Kuntz, S. J. Martens, and S. C. Warren, *Adv. Mater.* **31**, 1808213 (2019).
- [2] L. Daukiya, M. N. Nair, M. Cranney, F. Vonau, S. Hajjar-Garreau, D. Aubel, and L. Simon, *Prog. Surf. Sci.* **94**, 1 (2019).
- [3] J. Wan, S. D. Lacey, J. Dai, W. Bao, M. S. Fuhrer, and L. Hu, *Chem. Soc. Rev.* **45**, 6742 (2016).
- [4] N. Briggs, Z. M. Gebeyehu, A. Vera, T. Zhao, K. Wang, A. D. L. F. Duran, B. Bersch, T. Bowen, K. L. Knappenberger, and J. A. Robinson, *Nanoscale* **11**, 15440 (2019).
- [5] C. Riedl, C. Coletti, T. Iwasaki, A. A. Zakharov, and U. Starke, *Phys. Rev. Lett.* **103**, 246804 (2009).
- [6] I. Gierz, T. Suzuki, R. T. Weitz, D. S. Lee, B. Krauss, C. Riedl, U. Starke, H. Höchst, J. H. Smet, C. R. Ast, and K. Kern, *Phys. Rev. B* **81**, 235408 (2010).
- [7] S. Oida, F. R. McFeely, J. B. Hannon, R. M. Tromp, M. Copel, Z. Chen, Y. Sun, D. B. Farmer, and J. Yurkas, *Phys. Rev. B* **82**, 041411(R) (2010).
- [8] S. L. Wong, H. Huang, Y. Wang, L. Cao, D. Qi, I. Santoso, W. Chen, and A. T. S. Wee, *ACS Nano* **5**, 7662 (2011).
- [9] J. Sforzini, L. Nemeč, T. Denig, B. Stadtmüller, T.-L. Lee, C. Kumpf, S. Soubatch, U. Starke, P. Rinke, V. Blum, F. C. Bocquet, and F. S. Tautz, *Phys. Rev. Lett.* **114**, 106804 (2015).
- [10] J. L. McChesney, A. Bostwick, T. Ohta, T. Seyller, K. Horn, J. González, and E. Rotenberg, *Phys. Rev. Lett.* **104**, 136803 (2010).
- [11] K. Kanetani, K. Sugawara, T. Sato, R. Shimizu, K. Iwaya, T. Hitosugi, and T. Takahashi, *Proc. Natl. Acad. Sci. USA* **109**, 19610 (2012).
- [12] K. Li, X. Feng, W. Zhang, Y. Ou, L. Chen, K. He, L.-L. Wang, L. Guo, G. Liu, Q.-K. Xue, and X. Ma, *Appl. Phys. Lett.* **103**, 062601 (2013).
- [13] R. Shimizu, K. Sugawara, K. Kanetani, K. Iwaya, T. Sato, T. Takahashi, and T. Hitosugi, *Phys. Rev. Lett.* **114**, 146103 (2015).
- [14] S. Ichinokura, K. Sugawara, A. Takayama, T. Takahashi, and S. Hasegawa, *ACS Nano* **10**, 2761 (2016).
- [15] B. M. Ludbrook, G. Levy, P. Nigge, M. Zonno, M. Schneider, D. J. Dvorak, C. N. Veenstra, S. Zhdanovich, D. Wong, P. Dosanjh, C. Straßer, A. Stöhr, S. Forti, C. R. Ast, U. Starke, and A. Damascelli, *Proc. Natl. Acad. Sci. USA* **112**, 11795 (2015).
- [16] J. A. Robinson, M. Hollander, M. LaBella, K. A. Trumbull, R. Cavalero, and D. W. Snyder, *Nano Lett.* **11**, 3875 (2011).
- [17] S. Tanabe, M. Takamura, Y. Harada, H. Kageshima, and H. Hibino, *Appl. Phys. Express* **5**, 125101 (2012).
- [18] S. Forti, A. Stöhr, A. A. Zakharov, C. Coletti, K. V. Emtsev, and U. Starke, *2D Mater.* **3**, 035003 (2016).
- [19] M. Kim, M. C. Tringides, M. T. Hershberger, S. Chen, M. Hupalo, P. A. Thiel, C.-Z. Wang, and K.-M. Ho, *Carbon* **123**, 93 (2017).
- [20] Y. R. Niu, A. A. Zakharov, and R. Yakimova, *Ultramicroscopy* **183**, 49 (2017).
- [21] P. Rosenzweig, H. Karakachian, S. Link, K. Küster, and U. Starke, *Phys. Rev. B* **100**, 035445 (2019).
- [22] H. Kim, O. Dugerjav, A. Lkhagvasuren, and J. M. Seo, *Carbon* **144**, 549 (2019).

- [23] S. Forti, S. Link, A. Stöhr, Y. Niu, A. A. Zakharov, C. Coletti, and U. Starke, *Nat. Commun.* **11**, 2236 (2020).
- [24] Y. Endo, Y. Fukaya, I. Mochizuki, A. Takayama, T. Hyodo, and S. Hasegawa, *Carbon* **157**, 857 (2020).
- [25] Y. Zhang, H. Zhang, Y. Cai, J. Song, D. Qiao, Q. Chen, F. Hu, P. Wang, K. Huang, and P. He, *Chem. Phys. Lett.* **703**, 33 (2018).
- [26] J. C. Kotsakidis, A. Grubišić-Čabo, Y. Yin, A. Tadich, R. L. Myers-Ward, M. DeJarld, S. P. Pavunny, M. Currie, K. M. Daniels, C. Liu, M. T. Edmonds, N. V. Medhekar, D. K. Gaskill, A. L. Vázquez de Parga, and M. S. Fuhrer, *Chem. Mater.* **32**, 6464 (2020).
- [27] Y. Han, A. Lii-Rosales, Y. Zhou, C.-J. Wang, M. Kim, M. C. Tringides, C.-Z. Wang, P. A. Thiel, and J. W. Evans, *Phys. Rev. Materials* **1**, 053403 (2017).
- [28] A. Lii-Rosales, Y. Han, J. W. Evans, D. Jing, Y. Zhou, M. C. Tringides, M. Kim, C.-Z. Wang, and P. A. Thiel, *J. Phys. Chem. C* **122**, 4454 (2018).
- [29] A. Lii-Rosales, Y. Han, K. M. Yu, D. Jing, N. Anderson, D. Vaknin, M. C. Tringides, J. W. Evans, M. S. Altman, and P. A. Thiel, *Nanotechnology* **29**, 505601 (2018).
- [30] S. E. Julien, A. Lii-Rosales, K.-T. Wan, Y. Han, M. C. Tringides, J. W. Evans, and P. A. Thiel, *Nanoscale* **11**, 6445 (2019).
- [31] Y. Han, A. Lii-Rosales, M. C. Tringides, J. W. Evans, and P. A. Thiel, *Phys. Rev. B* **99**, 115415 (2019).
- [32] A. Lii-Rosales, Y. Han, K. C. Lai, D. Jing, M. C. Tringides, J. W. Evans, and P. A. Thiel, *J. Vac. Sci. Technol. A* **37**, 061403 (2019).
- [33] A. Lii-Rosales, Y. Han, S. E. Julien, O. Pierre-Louis, D. Jing, M. C. Tringides, K.-T. Wan, J. W. Evans, and P. A. Thiel, *New J. Phys.* **22**, 023016 (2020).
- [34] A. Lii-Rosales, Y. Han, D. Jing, M. C. Tringides, and P. A. Thiel, *Phys. Rev. Research* **2**, 033175 (2020).
- [35] A. Lii-Rosales, Y. Han, D. Jing, M. C. Tringides, S. Julien, K.-T. Wan, C.-Z. Wang, K. C. Lai, J. W. Evans, and P. A. Thiel, *Nanoscale* **13**, 1485 (2021).
- [36] N. A. Anderson, M. Hupalo, D. Keavney, M. C. Tringides, and D. Vaknin, *Phys. Rev. Materials* **1**, 054005 (2017).
- [37] N. A. Anderson, M. Hupalo, D. Keavney, M. Tringides, and D. Vaknin, *J. Mag. Mag. Mater.* **474**, 666 (2019).
- [38] G. Kresse and J. Furthmüller, *Phys. Rev. B* **54**, 11169 (1996).
- [39] G. Kresse and D. Joubert, *Phys. Rev. B* **59**, 1758 (1999).
- [40] J. Klimeš, D. R. Bowler, and A. Michaelides, *J. Phys.: Condens. Mater* **22**, 022201 (2010).
- [41] Y. Han, K. C. Lai, A. Lii-Rosales, M. C. Tringides, J. W. Evans, and P. A. Thiel, *Surf. Sci.* **685**, 48 (2019).
- [42] Y. Han, M. C. Tringides, J. W. Evans, and P. A. Thiel, *Phys. Rev. Research* **2**, 013182 (2020).
- [43] W. Li, L. Huang, M. C. Tringides, J. W. Evans, and Y. Han, *J. Phys. Chem. Lett.* **11**, 9725 (2020).
- [44] G. Henkelman and H. Jónsson, *J. Chem. Phys.* **113**, 9978 (2000).
- [45] I. Forbeaux, J.-M. Themlin, and J.-M. Debever, *Phys. Rev. B* **58**, 16396 (1998).
- [46] T. Ohta, A. Bostwick, T. Seyller, K. Horn, and E. Rotenberg, *Science* **313**, 951 (2006).
- [47] A. Mattausch and O. Pankratov, *Phys. Rev. Lett.* **99**, 076802 (2007).
- [48] S. J. Sung, J. W. Yang, P. R. Lee, J. G. Kim, M. T. Ryu, H. M. Park, G. Lee, C. C. Hwang, K. S. Kim, J. S. Kim, and J. W. Chung, *Nanoscale* **6**, 3824 (2014).
- [49] F. Bisti, G. Profeta, H. Vita, M. Donarelli, F. Perrozzi, P. M. Sheverdyaeva, P. Moras, K. Horn, and L. Ottaviano, *Phys. Rev. B* **91**, 245411 (2015).
- [50] N. M. Caffrey, R. Armiento, R. Yakimova, and I. A. Abrikosov, *Phys. Rev. B* **92**, 081409(R) (2015).
- [51] Y. Han, A. Lii-Rosales, M. C. Tringides, and J. W. Evans, *J. Chem. Phys.* **154**, 024703 (2021).
- [52] Y. Han, J. W. Evans, and M. C. Tringides, *Appl. Phys. Lett.* **119**, 033101 (2021).
- [53] T. A. de Jong, E. E. Krasovskii, C. Ott, R. M. Tromp, S. J. van der Molen, and J. Jobst, *Phys. Rev. Materials* **2**, 104005 (2018).
- [54] B. Butz, C. Dolle, F. Niekiel, K. Weber, D. Waldmann, H. B. Weber, B. Meyer, and E. Spiecker, *Nature* **505**, 533 (2014).
- [55] J. S. Alden, A. W. Tsen, P. Y. Huang, R. Hovden, L. Brown, J. Park, D. A. Muller, and P. L. McEuen, *Proc. Natl. Acad. Sci. USA* **110**, 11256 (2013).
- [56] H. Hibino, S. Mizuno, H. Kageshima, M. Nagase, and H. Yamaguchi, *Phys. Rev. B* **80**, 085406 (2009).
- [57] See Supplemental Material at <http://link.aps.org/supplemental/10.1103/PhysRevMaterials.5.074004> for DFT data in Figs. 3, 4, 6–8, 10, and 11 as well as additional DFT calculations for energy landscape of a Dy atom from top to BT gallery of a graphene-SiC system with stepped TLG.
- [58] J. W. Evans, P. A. Thiel, and M. C. Bartelt, *Surf. Sci. Rep.* **61**, 1 (2006).
- [59] J. W. Evans, Y. Han, B. Ünal, M. Li, K. J. Caspersen, D. Jing, A. R. Layson, C. R. Stoldt, T. Duguet, and P. A. Thiel, *AIP Conf. Proc.* **1270**, 26 (2010).
- [60] Y. Han, J. W. Evans, and F. Liu, *Phys. Rev. B* **100**, 195405 (2019).
- [61] F. Birch, *Phys. Rev.* **71**, 809 (1947).
- [62] F. D. Murnaghan, *Proc. Natl. Acad. Sci. USA* **30**, 244 (1944).
- [63] A. Bauer, P. Reischauer, J. Kräusslich, N. Schell, W. Matz, and K. Goetz, *Acta Cryst. A* **57**, 60 (2001).
- [64] G. C. Capitani, S. D. Pierro, and G. Tempesta, *Am. Mineral.* **92**, 403 (2007).
- [65] W. A. Bassett, M. S. Weathers, and T.-C. Wu, *J. Appl. Phys.* **74**, 3824 (1993).
- [66] R. Hill, *Proc. Phys. Soc. A* **65**, 349 (1952).
- [67] K. Kamitani, M. Grimsditch, J. C. Nipko, and C.-K. Loong, *J. Appl. Phys.* **82**, 3152 (1997).
- [68] V. Baskin and L. Meyer, *Phys. Rev.* **100**, 544 (1955).
- [69] C. Kittel, *Introduction to Solid State Physics*, 7th ed. (Wiley, New York, 1996).
- [70] M. H. Gass, U. Bangert, A. L. Bleloch, P. Wang, R. R. Nair, and A. K. Geim, *Nat. Nanotechnol.* **3**, 676 (2008).
- [71] J. R. Banister, T. S. Legvold, and F. H. Spedding, *Phys. Rev.* **94**, 1140 (1954).
- [72] O. C. Trulson, Ph.D. Dissertation, Iowa State University, 1959.
- [73] X. Liu, Y. Han, J. W. Evans, A. K. Engstfeld, R. J. Behm, M. C. Tringides, M. Hupalo, H.-Q. Lin, L. Huang, K.-M. Ho, D. Appy, P. A. Thiel, and C.-Z. Wang, *Prog. Surf. Sci.* **90**, 397 (2015).